


# Spinal Cord Synaptic Plasticity by GlyR $\beta$ Release from Receptor Fields and Syndapin I-Dependent Uptake

 Jessica Tröger,<sup>1</sup>  Eric Seemann,<sup>1</sup> Rainer Heintzmann,<sup>2,3</sup> Michael M. Kessels,<sup>1</sup> and Britta Qualmann<sup>1</sup>

<sup>1</sup>Institute of Biochemistry I, Jena University Hospital/Friedrich Schiller University Jena, Jena 07743, Germany, <sup>2</sup>Leibniz Institute of Photonic Technology, Jena 07745, Germany, and <sup>3</sup>Institute of Physical Chemistry and Abbe Center of Photonics, Friedrich-Schiller-University, Jena 07745, Germany

Glycine receptor-mediated inhibitory neurotransmission is key for spinal cord function. Recent observations suggested that by largely elusive mechanisms also glycinergic synapses display synaptic plasticity. We imaged receptor fields at ultrahigh-resolution at freeze-fractured membranes, tracked surface and internalized glycine receptors (GlyR), and studied differential regulations of GlyR $\beta$  interactions with the scaffold protein gephyrin and the F-BAR domain protein syndapin I and thereby reveal key principles of this process. S403 phosphorylation of GlyR $\beta$ , known to be triggered by synaptic signaling, caused a decoupling from gephyrin scaffolds but simultaneously promoted association of syndapin I with GlyR $\beta$ . In line, kainate treatments used to trigger rearrangements of glycine receptors in murine *syndapin I* KO spinal cords (mixed sex) showed even more severe receptor field fragmentation than already observed in untreated *syndapin I* KO spinal cords. Syndapin I deficiency furthermore resulted in more dispersed receptors and increased receptor mobility, also pointing out an important contribution of syndapin I to the organization of GlyR $\beta$  fields. Strikingly, *syndapin I* KO also led to a complete disruption of kainate-induced GlyR $\beta$  internalization. Accompanying quantitative ultrahigh-resolution studies in dissociated spinal cord neurons proved that the defects in GlyR internalization observed in *syndapin I* KO spinal cords are neuron-intrinsic defects caused by syndapin I deficiency. Together, our results unveiled important mechanisms organizing and altering glycine receptor fields during both steady state and particularly also as a consequence of kainate-induced synaptic rearrangement - principles organizing and fine-tuning synaptic efficacy and plasticity of glycinergic synapses in the spinal cord.

**Key words:** freeze-fracturing and electron microscopy; glycine receptor beta phosphorylation; high and ultrahigh-resolution imaging of glycine receptor fields; kainate-induced glycine receptor beta internalization; spinal cord; synaptic plasticity.

## Significance Statement

Initial observations suggested that also glycinergic synapses, key for spinal cord and brainstem functions, may display some form of synaptic plasticity. Imaging receptor fields at ultrahigh-resolution at freeze-fractured membranes, tracking surface and internalized glycine receptors (GlyR) and studying regulations of GlyR $\beta$  interactions, we here reveal key principles of these kainate-inducible adaptations. A switch from gephyrin-mediated receptor scaffolding to syndapin I-mediated GlyR $\beta$  scaffolding and internalization allows for modulating synaptic receptor availability. In line, kainate-induced GlyR $\beta$  internalization was completely disrupted and GlyR $\beta$  receptor fields were distorted by *syndapin I* KO. These results unveiled important mechanisms during both steady-state and kainate-induced alterations of synaptic GlyR fields, principles underlying synaptic efficacy and plasticity of synapses in the spinal cord.

Received Oct. 13, 2021; revised June 23, 2022; accepted July 13, 2022.

Author contributions: J.T., E.S., M.M.K., and B.Q. designed research; J.T. and E.S. performed research; J.T. and E.S. analyzed data; J.T., M.M.K., and B.Q. wrote the first draft of the paper; J.T., R.H., M.M.K., and B.Q. edited the paper; J.T., M.M.K., and B.Q. wrote the paper; R.H. contributed unpublished reagents/analytic tools.

This work was supported by Deutsche Forschungsgemeinschaft Grants QU116/9-1 to B.Q. and TRR166 Project B05 to B.Q. and R.H. We thank Susanne Berr, Kristin Gluth, Annett Kreuzsch, Michaela Öhler, Birgit Schade, Nicole Koch, and Christian Karras for technical support; Martin Westermann for access to freeze-fracturing and TEM; and Ingo Paarmann and Heinrich Betz for providing plasmids encoding for GFP-GlyR $\beta$  and GFP-gephyrin.

The authors declare no competing financial interests.

Correspondence should be addressed to Michael M. Kessels at Michael.Kessels@med.uni-jena.de or Britta Qualmann at Britta.Qualmann@med.uni-jena.de.

<https://doi.org/10.1523/JNEUROSCI.2060-21.2022>

Copyright © 2022 the authors

## Introduction

Inhibitory neurotransmission in spinal cord and brainstem mainly is glycine receptor (GlyR)-mediated. Postsynaptic GlyRs are heteromeric pentamers containing  $\alpha_1$ - $\alpha_4$  and  $\beta$  subunits, whereas homomeric GlyRs (5  $\alpha$ -subunits) can also be found as extrasynaptic reservoir (Legendre et al., 2002; Dutertre et al., 2012). Synaptic receptor arrays are formed by the scaffolding protein gephyrin (Kirsch and Betz, 1995), which interacts tightly with  $\beta$  subunits (GlyR $\beta$ ) (Grudzinska et al., 2005; Dumoulin et al., 2010; Alvarez, 2017; Kasaragod and Schindelin, 2018).

Synaptic strength can be modulated by changes of the amount of neurotransmitter receptors in the postsynaptic membrane.

Whereas mechanisms of synaptic plasticity are well understood for glutamate receptors in excitatory synapses in the hippocampus (Diering and Haganir, 2018; Choquet and Hosy, 2020), mechanisms that modulate the activity of inhibitory synapses in spinal cord and brainstem are far less understood. The activation of NMDA receptors was observed to decrease lateral GlyR diffusion, to increase GlyR cluster number, and to correspondingly result in higher amplitudes of glycinergic mIPSCs (Lévi et al., 2008). In contrast, activation of PKC, for example, via kainate receptor stimulation, led to (1) increased lateral GlyR diffusion, (2) decreased GlyR abundance at inhibitory synapses, and (3) S403 phosphorylation in the cytoplasmic loop of GlyR $\beta$  reducing gephyrin binding (Specht et al., 2011). Kainate stimulation also led to GlyR endocytosis (Sun et al., 2014). This modulation of receptor surface availability also was reported to be PKC-dependent. It resulted in dramatic reductions of GlyR puncta in cultured spinal cord neurons (Sun et al., 2014). Yet, apart from the apparently required decoupling from gephyrin, the organizational changes of inhibitory receptor arrays and components that are critical for GlyR dynamics largely remained elusive.

The large intracellular loop of GlyR $\beta$  binds to the membrane-binding F-BAR protein syndapin I (also called PACSIN1) (Qualmann et al., 1999, 2011; Kessels and Qualmann, 2015) at a site distinct from but adjacent to the gephyrin binding site; and syndapin I deficiency was reported to cause some reduction of GlyR puncta (del Pino et al., 2014). A GlyR $\alpha$  mutation, which coincided with reduced syndapin I interaction in *in vitro*-reconstitution screenings with GlyR peptides, was accompanied by startle disease and showed disturbed glycinergic neurotransmission (Langlhofer et al., 2020).

Here we demonstrate by (ultra)high-resolution analyses of spinal cords that *syndapin I* KO does not lead to a reduction of GlyR $\beta$  at the plasma membrane but to fragmentations of GlyR fields. Syndapin I deficiency also increased GlyR $\beta$  mobility. Under kainate stimulation, the pivotal role of syndapin I in the organization of GlyR fields and in the modulation of GlyR availability became even more visible. Regulatory mechanisms, which decouple GlyR $\beta$  subunits from gephyrin, promoted GlyR $\beta$ /syndapin I interactions. Furthermore, syndapin I was identified as crucial for GlyR internalization during kainate-induced reorganization.

Our work highlights a critical element in glycine receptor field organization and in the thus far poorly understood kainate-induced GlyR $\beta$  dynamics of inhibitory synapses.

## Materials and Methods

**Mice.** The generation of *syndapin I* KO mice has been described previously (Koch et al., 2011). For preparation of primary spinal cord neurons, WT and *syndapin I* KO embryos (E14; mixed sex) derived from heterozygous breedings were used. All animal procedures were approved by the local government (Thüringer Landesamt and Landesverwaltungsamt; breeding allowance UKJ-17-021).

**Plasmids and recombinant proteins.** Plasmids encoding for GFP and GST fusion proteins of syndapin I and syndapin I SH3 domain as well as the preparation of GST fusion proteins have been described previously (Qualmann et al., 1999; Kessels and Qualmann, 2006).

Plasmids encoding for GST fusion proteins of GlyR $\beta$  (aa378–455) and of the E domain of gephyrin (aa316–736) as well as GFP-GlyR $\beta$  and GFP-gephyrin were kind gifts of I. Paarmann (Sola et al., 2004). GFP-GlyR $\beta$  cytoplasmic loop (aa378–455) as well as GFP-gephyrin E domain were subcloned from the corresponding GST fusion constructs.

In order to generate a gephyrin E domain without any tag, the E domain was subcloned into pGEX-6P-1 (GE Healthcare). The GST-gephyrin E domain fusion protein was purified from *Escherichia coli*,

and the GST-tag used for protein purification was cleaved off according to procedures described previously (Wolf et al., 2019).

GST-GlyR $\beta$  cytoplasmic loop (aa378–455) S403A and GST-GlyR $\beta$  cytoplasmic loop S403E mutants were generated using site-directed mutagenesis with the following primers, 5'-TTCAGCATTGTTGGCGCC TTACCAAGAGATT-3' and 5'-AAATCTCTTGGTAAGGCCGCCAA CAATGCTGAA-3' for S403A and 5'-TTCAGCATTGTTGGCGAGT TACCAAGAGATT-3' and 5'-AAATCTCTTGGTAACTCGCCAAC AATGCTGAA-3' for S403E, respectively.

*Syndapin I* RNAi plasmids and a scrambled control (pRNAT backbone) were established previously (Dharmalingam et al., 2009). The plasmid versions used additionally encoded for farnesylated mCherry as fluorescent reporter (Schneider et al., 2014).

**Antibodies.** Polyclonal rabbit antibodies against syndapin I (#2704) and their affinity purification were described previously (Qualmann et al., 1999). The same antiserum was used to purify polyclonal antibodies against GST (Qualmann et al., 1999). Polyclonal guinea pig antibodies against GST were purified from antisera as described previously (Braun et al., 2005).

Monoclonal mouse antibodies against GlyR (extracellular; clone mAb4a; #146011; RRID:AB\_887722) and GlyR $\beta$  (intracellular epitope; clone 299E7; #146211; RRID:AB\_2619833) used for immunofluorescence stainings and EM studies were from Synaptic Systems. Polyclonal rabbit anti-GlyR $\beta$  (#15371-1-AP; RRID:AB\_2878132) used for Western blot analysis was purchased from Proteintech and polyclonal rabbit anti-gephyrin antibodies (#PA5-19589; RRID:AB\_10984155) from Thermo Fisher Scientific. Polyclonal guinea pig anti-MAP2 antibodies (#188004; RRID:AB\_2138181) used for immunofluorescence stainings as well as the polyclonal guinea pig anti-VGAT antiserum (#SYSY131004; RRID:AB\_887873) were from Synaptic Systems. Mouse monoclonal anti-SMI-32 antibodies (#801701; RRID:AB\_2564642) were purchased from BioLegend and mouse monoclonal anti-MAP2 (clone HM-2; M9942; RRID:AB\_477256) from Sigma. Monoclonal anti-GFP antibodies (clone JL-8; lot #A5033481-A; RRID:AB\_10013427) were from Clontech Takara Bio, and polyclonal goat anti-GAPDH (sc-48167; RRID:AB\_1563046) was from Santa Cruz Biotechnology.

Alexa-488-, Alexa-568-, and Alexa-647-conjugated secondary antibodies against the different primary antibodies were purchased from Invitrogen (RRID:AB\_141607; RRID:AB\_2534013; RRID:AB\_2535792; RRID:AB\_2735091). Secondary antibodies for immunoblotting included DyLight800-conjugated goat anti-mouse and anti-rabbit antibodies (Thermo Fisher Scientific; RRID:AB\_2556774 und RRID:AB\_2556775) as well as donkey anti-guinea pig IRDye 680 (RRID:AB\_10956079), anti-guinea pig IRDye800 conjugates (LI-COR Biosciences; RRID:AB\_1850024), AlexaFluor-680-labeled goat anti-mouse and anti-rabbit antibodies (Thermo Fisher Scientific; RRID:AB\_2535758 and RRID:AB\_1965956) as well as AlexaFluor-680-labeled donkey anti-goat antibody (Thermo Fisher Scientific; RRID:AB\_2535741). Secondary goat anti-mouse antibodies conjugated with 10 nm gold particles for EM studies were purchased from British Biocell International. Phalloidin-AlexaFluor-488 was from Thermo Fisher Scientific (#A12379).

**Mouse spinal cord homogenates and rat brain lysates.** Spinal cord homogenates of WT and *syndapin I* KO mice were obtained by using an IKA Ultra-Turrax homogenizer and 5 mM HEPES, pH 7.4, 0.32 M sucrose, Complete EDTA-free (Roche), and 1 mM EDTA as homogenization buffer. Homogenates were centrifuged at 1000  $\times$  g, and the postnuclear supernatants were used for immunoblotting analyses. To detect GlyR and gephyrin with sufficient sensitivity, incubations with sample buffer for SDS-PAGE were performed for 15 min at room temperature.

Rat brain lysates were generated as described previously (Haag et al., 2018; Wolf et al., 2019). In brief, adult rats were sacrificed and the brain was removed and homogenized in ice-cold 5 mM HEPES, pH 7.4, 0.32 M sucrose, 1 mM EDTA containing Complete EDTA-free protease inhibitors using a Potter S homogenizer (Sartorius). After addition of Triton X-100 (1% (v/v) final) and incubation for 20 min at 4°C, cell debris and nuclei were removed by centrifugation at 1000  $\times$  g.

Protein concentrations in homogenates and lysates were determined by BCA assays and used to ensure equal loadings of different samples in Western blotting analyses.

**Coprecipitation assays.** Transfection of HEK293 cells and preparation of HEK293 lysates were performed with 10 mM HEPES, pH 7.4, 1 mM EGTA, 0.1 mM MgCl<sub>2</sub>, 1% (v/v) Triton X-100, 150 mM NaCl, and Complete EDTA-free as lysis buffer as described previously (Schwintzer et al., 2011).

Coprecipitation experiments were done as described (Schneider et al., 2014). In brief, GST or GST fusion proteins of syndapin I and syndapin I SH3 domain, respectively, were coupled to a glutathione-matrix and incubated with lysates from HEK293 cells overexpressing GFP-GlyR $\beta$  and deletion mutants thereof and, for endogenous coprecipitation studies, with rat brain lysates generated as described above, respectively. After washing, bound proteins were eluted by incubation for 30 min at room temperature in elution buffer (20 mM glutathione, 120 mM NaCl, 50 mM Tris/HCl, pH 8.0). The resulting samples were analyzed by immunoblotting using a LI-COR Odyssey system (LI-COR Biosciences).

For tertiary complex analysis, purified gephyrin E domain was added in increasing amounts to incubations with immobilized GST and GST-syndapin I SH3 and lysates of HEK293 cells expressing GFP-GlyR $\beta$  cytoplasmic loop. Eluates and supernatants were analyzed by immunoblotting with antibodies visualizing all three components.

For examinations of the influence of the S403 PKC phosphorylation site, purified GST fusion proteins of GlyR $\beta$  cytoplasmic loop S403A and GlyR $\beta$  cytoplasmic loop S403E mutants were immobilized and incubated with lysates from HEK293 cells transfected with GFP-syndapin I or GFP-gephyrin E domain. Eluates and supernatants were analyzed by quantitative immunoblotting using a LI-COR Odyssey system.

**Cultures of primary mouse spinal cord neurons.** Preparations of dissociated mouse spinal cord neurons from embryonic day 14 embryos were done as described (Grosskreutz et al., 2007) with minor changes. In brief, embryos were taken out, decapitated, and biopsied for genotyping. WT and KO embryos were pooled. Ventral horns of the spinal cords were prepared in ice-cold HBSS, trypsinized with 0.05% (w/v) trypsin/EDTA (Invitrogen) for 20 min at 37°C, and triturated after treatment with DNaseI in plating medium (1% (v/v) horse serum, 33 mM glucose in MEM (Invitrogen)).

Neurons were grown on 18 mm coverslips coated with poly-L-lysine and paraffin droplets in plating medium for 45 min. Subsequent to cell settlement, the coverslips were turned upside-down and maintained in Neurobasal A medium (Invitrogen) containing 1 $\times$  B27 supplement, 1 $\times$  N2 supplement, 2 mM GlutaMax (Invitrogen), 2% (v/v) horse serum, 2 ng/ml BDNF, 100 U/ml penicillin, and 100  $\mu$ g/ml streptomycin. After 2 d in culture, cytosine-1- $\beta$ -D-arabinofuranoside (Sigma) was added to minimize glial cells (final concentration 1  $\mu$ M). Spinal cord neurons were grown at 37°C and 5% humidity until usage.

**Immunofluorescence analyses.** Spinal cord neurons were fixed in 4% (w/v) PFA in PBS, pH 7.4, at room temperature for ~4 min and permeabilized in blocking buffer (10% (v/v) horse serum, 5% (w/v) BSA in PBS with 0.2% (v/v) Triton X-100) as described for hippocampal neurons (Koch et al., 2020). Spinal cord neurons grown on poly-L-lysine-coated sapphire discs (see freeze-fracture experiments) were subjected to immunofluorescence analyses in a similar manner.

Antibody solutions were prepared in blocking buffer without Triton X-100. Neurons were incubated with primary antibodies overnight at 4°C and washed 3 times with blocking buffer. Then, secondary antibodies were applied for 1 h at room temperature. After final washing steps and DAPI staining (5 min, 1:10,000 in PBS), coverslips were mounted onto glass slides using Mowiol 28-99 (#10849, Sigma).

**Quantitative fluorescent image analyses of gephyrin and GlyR cluster organization.** Images of spinal cord neurons of syndapin I KO and WT mice were recorded as *z* series with 0.25–0.3  $\mu$ m intervals using a Zeiss AxioObserver Z1 microscope equipped with an ApoTome2 (Zeiss) as well as with a high-resolution structured illumination microscope (Zeiss ELYRA S1), respectively. An ApoTome creates optical sections of fluorescent samples via structured illumination (a linear grid moved into the light path at three different positions in three consecutive images) to remove of out-of-focus light to generate a pseudo-confocal image at normal light microscopical resolution, whereas high-resolution structured illumination microscopes, such as the ELYRA S1 (Zeiss), provide image resolutions up to ~100 nm (Tröger et al., 2020).

Maximum intensity projections (MIPs) of both apotome and structured illumination microscopy (SIM) images were processed equally and were quantitatively analyzed by Imaris 8.4 software (Bitplane; RRID:SCR\_007370) using the tools *surface* (generation of clusters) and *filament* (rebuild dendrite structure). Statistical parameters, such as cluster surface, number of clusters per filament length, and mean intensity in glycine receptor clusters were explored from the generated reconstructions. Analyses of gephyrin clusters were done accordingly. Evaluations of gephyrin clusters overlapping with GlyR clusters were based on colabelings of gephyrin and GlyR $\beta$  and the corresponding 3D-reconstructions using Imaris 8.4 (Bitplane; RRID:SCR\_007370).

All analyses of spinal cord neurons were performed with several independent neuronal preparations. Twenty SIM images of dendrite segments and cells each (WT/KO) and 34 (WT) and 36 (KO) ApoTome images were evaluated for cluster density determinations. From these images, 10184 (WT) and 12855 (KO) and 7144 (WT) and 7234 (KO) individual GlyR $\beta$  clusters were analyzed for GlyR $\beta$ . The data were derived from three independent preparations from 3 + 8 + 8 WT pooled embryos and 4 + 3 + 11 pooled KO embryos, respectively. For gephyrin analyses, 21 (WT) and 23 (KO) cells of two independent neuronal preparations were analyzed for cluster densities, and 9372 (WT) and 11982 (KO) gephyrin clusters were evaluated by parallel anti-gephyrin immunostainings.

Anti-gephyrin immunostaining in relation to anti-GlyR $\beta$  immunodetection was analyzed for 10184/12855 (WT/KO) clusters (overall analyses) and for 1397/1389 (WT/KO) (large) and 8787/11466 (WT/KO) (small) GlyR clusters, respectively.

**Antibody internalization assays for demonstrating GlyR internalization.** For labeling surface-localized receptors, spinal cord neurons at DIV21/DIV22 were incubated with an antibody against an extracellular epitope of GlyR (mAb4a; pan anti-GlyR) for 15 min at 37°C in conditioned medium. After washing off excessive antibodies, neurons were treated with kainate (200  $\mu$ M) for 1 min to induce receptor internalization. The neurons were then incubated in conditioned medium for another 10 min, fixed with 4% PFA in PBS for 15 min, and stained with an Alexa-488-coupled secondary antibody detecting the primary anti-GlyR antibody overnight at 4°C in blocking buffer without Triton X-100 to label the surface receptor pool.

Subsequently, cells were fixed again (4% PFA, 10 min), permeabilized, and incubated with an Alexa-568-coupled secondary antibody for 1 h at room temperature to detect the internalized GlyR pool. Receptor internalization data were expressed as ratios of detected surface receptors and internalized receptors, as used for AMPAR analyses during long-term synaptic depression analyses (Koch et al., 2020). MAP2 counterstaining was used to visualize the dendrites of spinal cord neurons.

Sum intensities of immunolabeled receptor detected by either Alexa-488- or Alexa-568-conjugated secondary antibodies were quantified by using ImageJ (National Institutes of Health; RRID:SCR\_003070). Two dendritic segments were analyzed per cell, and their mean was used for calculating the internalization rates of an *n* of 46–66 cells per each condition.

**GFP-GlyR $\beta$  tracking in rat spinal neurons and quantitative analyses thereof.** For tracking experiments, rat spinal cord neurons were prepared as described for mouse spinal cord cultures with slight differences. In brief, neurons were dissociated from E18 rat embryos and plated on 18 mm coverslips coated with poly-D-lysine. The transfections were conducted at DIV14 with farnesylated mCherry-encoding vectors coexpressing syndapin I RNAi or a scrambled RNAi sequence as well as with GFP-GlyR $\beta$ . Time-lapse measurements of living transfected spinal cord neurons were performed 48 h later using a motorized Zeiss AxioObserver equipped with a spinning disc unit, an incubator, and an EMCCD camera, as described previously (Izadi et al., 2018). In brief, the medium was exchanged for live imaging buffer adjusted to iso-osmolarity by using a freezing point osmometer (Osmomat 3000; Gonotec) and 3D live imaging was conducted by recoding a full *z* series every 1 s over a time span of 15 min.

Neuronal morphologies were highlighted by using the plasma membrane-targeted mCherry coexpressed by the pRNAT plasmids used for syndapin RNAi and control, respectively, and by using Imaris 8.4

reconstruction software. Receptors along dendrites were reconstructed as spots (generation of spheres) and then tracked over time using Imaris 8.4. The GFP-GlyR $\beta$  cluster speeds and the displacement lengths in spinal cord neurons cotransfected with either syndapin I RNAi and control (scrambled RNAi) plasmids were determined from  $n = 1634$  tracks from 10 neurons (scrambled RNAi) and 2251 tracks from 11 neurons (syndapin I RNAi) from several independent neuronal preparations and coverslips.

**Spinal cord fixation, freeze-fracturing, immunogold labeling and EM.** Spinal cords dissected from WT and *syndapin I* KO mice were fixed by adding 1% (w/v) PFA in PBS overnight. The spinal cords were then cut perpendicularly, and the tissue blocks were subsequently cut longitudinally in 300  $\mu\text{m}$ -thick slices using a McIlwain Tissue Chopper. Samples from the ventral side were processed for freeze-fracturing.

In some experiments, spinal cord tissue isolated from WT and *syndapin I* KO mice, respectively, was incubated with 1 mM kainate in Krebs-Henseleit buffer (KHB; 11.1 mM D-glucose, 0.9 mM MgSO<sub>4</sub>, 1.3 mM KH<sub>2</sub>PO<sub>4</sub>, 4.7 mM KCl, 118.2 mM NaCl, 2.5 mM CaCl<sub>2</sub>, 25 mM NaHCO<sub>3</sub>, pH 7.2) for 1 h at 37°C. The tissue was then washed with KHB and pre-fixed in 1% PFA (w/v) in PBS, cut, and processed further for freeze-fracturing.

For some further spinal cord tissue samples, the kainate incubation was done with 200  $\mu\text{M}$  kainate in KHB for 10 min at 37°C. Controls were incubated in KHB without kainate for the respective time.

As preparation for freeze-fracturing, the sections were transferred into PBS and frozen between a copper sandwich profile by plunge freezing using a propane/ethane mix cooled by liquid nitrogen. The copper sandwiches were then subjected to freeze-fracturing and to shadowing with carbon and platinum/carbon (BAF 400, Balzers) following procedures described previously (Koch et al., 2012; Schneider et al., 2014). Resulting replica were incubated in 5% (w/v) SDS and 30 mM sucrose in 10 mM Tris/HCl, pH 8.4 at 60°C overnight. The cleaned replica were then washed with PBS.

Replica were immunolabeled in labeling and blocking buffer (1% (w/v) BSA, 0.5% (w/v) gelatin, and 0.0005% (v/v) Tween 20 in PBS) with mouse monoclonal anti-GlyR $\beta$  antibodies (intracellular epitope; clone 299E7; #146211) as primary antibodies (overnight, 4°C) and with 10 nm colloidal gold/anti-mouse conjugates as secondary antibodies (2 h, room temperature) similar to procedures previously described for different non-receptor proteins (Koch et al., 2012; Schneider et al., 2014; Seemann et al., 2017; Izadi et al., 2018; Wolf et al., 2019).

The immunogold-labeled samples were then analyzed by transmission electron microscopy (TEM) using an EM 902A (Zeiss) at 80 kV. Images were recorded digitally using a FastScan-CCD-camera (TVIPS camera and software).

Images were processed using Adobe Photoshop software.

For determinations of anti-GlyR $\beta$  labeling densities of freeze-fractured spinal cord tissue at steady state, 50/49 (WT/KO) images of freeze-fracture replica originating from each two independent spinal cord preparations (animals) were evaluated. For cluster analyses at steady state, all clusters (96/139 WT/KO) present on these images were examined.

The determinations of kainate stimulation effects on GlyR $\beta$  labeling densities, the densities of GlyR $\beta$  clusters, and of the dispersed anti-GlyR $\beta$  immunogold labeling in spinal cord tissue are based on 45–51 images (200  $\mu\text{M}$  kainate for 10 min) and 45–53 images (1 mM kainate for 60 min), respectively. All 76–239 individual clusters observed in the latter image set were evaluated individually for their anti-GlyR $\beta$  labeling density inside of the clusters and for their cluster areas.

**Preparation of cultured spinal cord neurons for freeze-fracturing and immunogold labeling.** For freeze-fracturing experiments and immunogold labeling of GlyR $\beta$  in dissociated cultured mouse neurons derived from spinal cords of WT and *syndapin I* KO mice (mixed sex), E14 spinal cords were prepared and dissociated as described above. The prepared primary cells were cultured on washed and poly-L-lysine-coated sapphire discs of 4 mm diameter for 20–21 d. The cells were then incubated with 200  $\mu\text{M}$  kainate for 1 min, as established for GlyR internalization assays (Sun et al., 2014) and as used for the immunofluorescence analyses (see above) or were left untreated (control). Subsequently, the cells were transferred into 20% (w/v) BSA in PBS and processed for

freeze-fracturing as described above. For determinations of anti-GlyR labeling densities, 42–66 images of freeze-fracture replica from neurons of at least two independent cultures and freeze-fracturing efforts were evaluated.

**Procedures and parameters of quantitative EM analyses.** Quantitative evaluations of immunogold signal densities were done by manual counting and by either considering the full images or individual, circular ROIs placed at anti-GlyR $\beta$  clusters (i.e., receptor fields). Areas were measured using ImageJ.

For receptor field analyses,  $\geq 3$  gold particles in close proximity were considered as a cluster, whereas not clustered immunolabelings (single, double) were counted as dispersed labeling. Gold particles with distances of  $> 50$  nm to the next particle inside of a cluster were not considered as part of the cluster during ROI placement. To ensure conservative measurements, rare cases of extraordinarily large irregular rather dumbbell-shaped clusters were considered as two separate areas, if labeling was sparse in a central area useful for dividing the irregular area into two circular areas. ROIs for measurements of receptor field sizes and for determinations of anti-GlyR $\beta$  labeling densities within receptor fields were placed in a way that they cover all immunogold signals of one cluster and have minimal diameter.

**Experimental design and statistical analyses.** All experiments were performed as three independent biological replicates (unless otherwise stated). All  $n$  numbers are noted in the figure legends. For quantitative Western blot analyses of GlyR $\beta$  and gephyrin expression levels, the respective immunosignals were normalized to anti-GADPH immunosignals. Except for Figure 1D,E, all quantitative data shown represent mean  $\pm$  SEM. Quantitative EM data are furthermore shown as bar/dot plot overlays to visualize all individual data points. Tests for normal data distribution and statistical significance calculation were done using GraphPad Prism 5 software (GraphPad Software, version 5.03; RRID:SCR\_002798).  $p$  values  $< 0.0001$  are not calculated by Prism 5 software.

**Data and software availability.** Full blots images are available in the Source data figures accompanying the respective figures in the manuscript. All numerical raw data are additionally available in Extended Data Figures 1–1, 2–1, 3–1, 4–1, 5–1, 6–1, 7–1, 8–1, 9–1, and 10–1.

## Results

### Binding of syndapin I and gephyrin to the cytoplasmic loop of GlyR $\beta$ is not mutually exclusive but shows partial competition

Using adjacent sites in the large cytoplasmic loop, GlyR $\beta$  interacts with both gephyrin and the membrane-binding protein syndapin I (del Pino et al., 2014). This raised the question whether these two proteins act independently in regulating GlyRs by competing with each other for binding or whether syndapin I and gephyrin may show some cooperative functions. Since syndapin I did not associate with gephyrin, neither when GFP-gephyrin overexpressed in HEK293 cells was offered nor when endogenous gephyrin from rat brain lysates was examined, but all gephyrin remained unbound in the supernatants (Fig. 1A,B), putative complex formations of syndapin I with gephyrin would only be indirect and GlyR $\beta$ -mediated.

Reconstitutions of complex formation with purified GST-syndapin I SH3 domain, GFP-tagged GlyR $\beta$ 's cytoplasmic loop expressed in HEK293 cells and purified, GlyR $\beta$ -binding gephyrin E domain (Fig. 1C–H) showed that increasing amounts of gephyrin E domain (Fig. 1C,D) diminished the amount of syndapin I SH3 domain-associated GlyR $\beta$  (Fig. 1C,E). Thus, there was considerable steric competition between the two different GlyR $\beta$  binding partners.

Yet, GFP-tagged GlyR $\beta$  cytoplasmic loop coprecipitated by immobilized syndapin I SH3 domain obviously also allowed for simultaneous association of some gephyrin E domain; that is, complexes of all three proteins were formed, too (Fig. 1C, arrowheads).

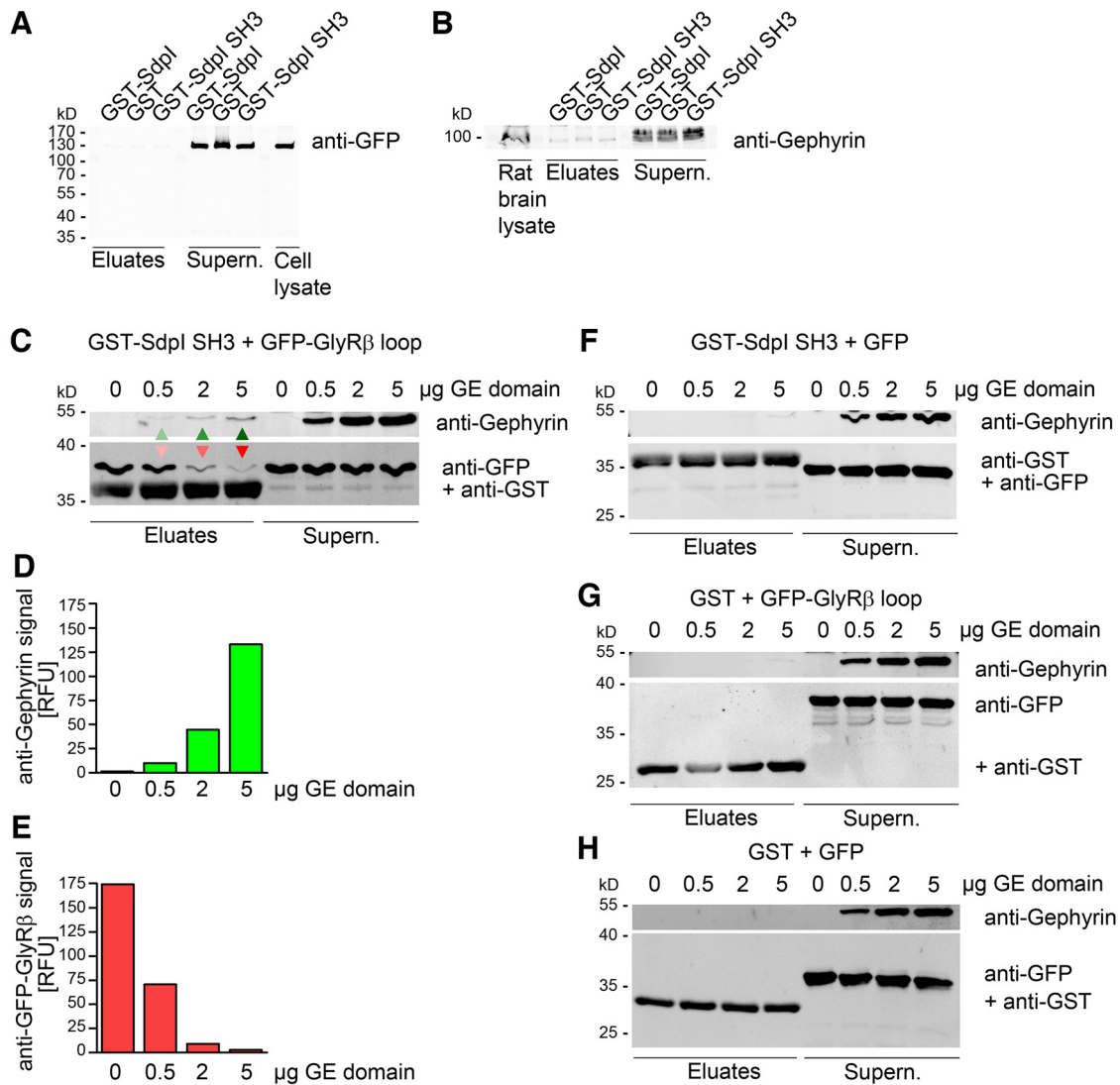


**Figure 1.** Binding of syndapin I and gephyrin to the cytoplasmic loop of GlyR $\beta$  is not mutually exclusive but shows partial competition. **A, B**, Immunoblotting analyses of attempts to coprecipitate GFP-gephyrin expressed in HEK293 cells (**A**) and endogenous gephyrin from rat brain lysates (**B**) with immobilized GST-syndapin I (GST-Sdpl) and GST-syndapin I SH3 domain (GST-Sdpl SH3) and GST (negative control) showing that syndapin I does not bind to gephyrin. Gephyrin remained in the supernatants (Supern.) in both experiments. **C–H**, Demonstration of complexes composed of GST-Sdpl SH3, GFP-GlyR $\beta$  cytoplasmic loop (GFP-GlyR $\beta$  loop), and gephyrin E (GE) domain by specific coprecipitation of gephyrin E domain by immobilized GST-Sdpl SH3 (**C,F**) but not by GST (**G,H**) in the presence of GFP-GlyR $\beta$  loop (**C**) but not in the absence of GlyR $\beta$  E-loop (GFP control; **F**). Green arrowheads indicate rising amounts of GE domain bound. Red arrowheads indicate the decrease of GST-Sdpl SH3-associated GFP-GlyR $\beta$  cytoplasmic loop by rising amounts of GE domain added. **D, E**, Quantitative visualization of rising amounts of gephyrin E domain (**D**) and decreasing amounts of GlyR $\beta$  bound to immobilized GST-syndapin I SH3 domain (**E**) at different concentrations of added GE domain. In addition to this competition, however, note that especially at the higher concentrations of GE domain tested, complexes composed of all three binding partners (Sdpl SH3, GlyR $\beta$  loop, and GE domain) were successfully formed (arrowheads) (**C**). For numerical data, see Extended Data Figure 1-1.

Together, the GlyR $\beta$  binding of syndapin I and gephyrin showed some, probably steric, competition but clearly was not mutually exclusive.

#### Increased microscopic resolution revealed that *syndapin I* KO does not lead to a reduced but instead to an increased density of smaller GlyR $\beta$ -containing receptor clusters

To shed light on a putative common, cooperative role of syndapin I and gephyrin in GlyR-mediated neurotransmission, we first focused on receptor scaffolding functions represented by gephyrin. Quantitative analyses of spinal cord homogenates showed that *syndapin I* KO did not lead to an alteration of the expression levels of GlyR $\beta$  when the expression of GlyR $\beta$  in *syndapin I* KO was compared with WT (Fig. 2*A,B*; not significant). This result was hard to reconcile with previous immunofluorescence analyses,

suggesting a reduced GlyR cluster density ( $\sim$ –20%) caused by *syndapin I* KO when a pan anti-GlyR antibody was used (del Pino et al., 2014). Intriguingly, high-resolution SIM unveiled that *syndapin I* KO did indeed not reduce the number of GlyR $\beta$  clusters along dendrites compared with WT neurons but instead increased them (Fig. 2*C,D*). The GlyR $\beta$  cluster density rose by  $\sim$ 27% (Fig. 2*E*;  $p = 0.0291$ ). Additionally, GlyR $\beta$  clusters of *syndapin I* KO spinal cord neurons were smaller than those of WT neurons (Fig. 2*F*;  $p < 0.0001$ ).

To address whether the gross discrepancy to literature data represented a lab-, reagent-, or experimenter-related inconsistency and/or a difference arising from the different microscopy techniques used, which may also have some major impact on the analysis of subcellular structures in the nervous system (Tröger et al., 2020), we analyzed the same samples as

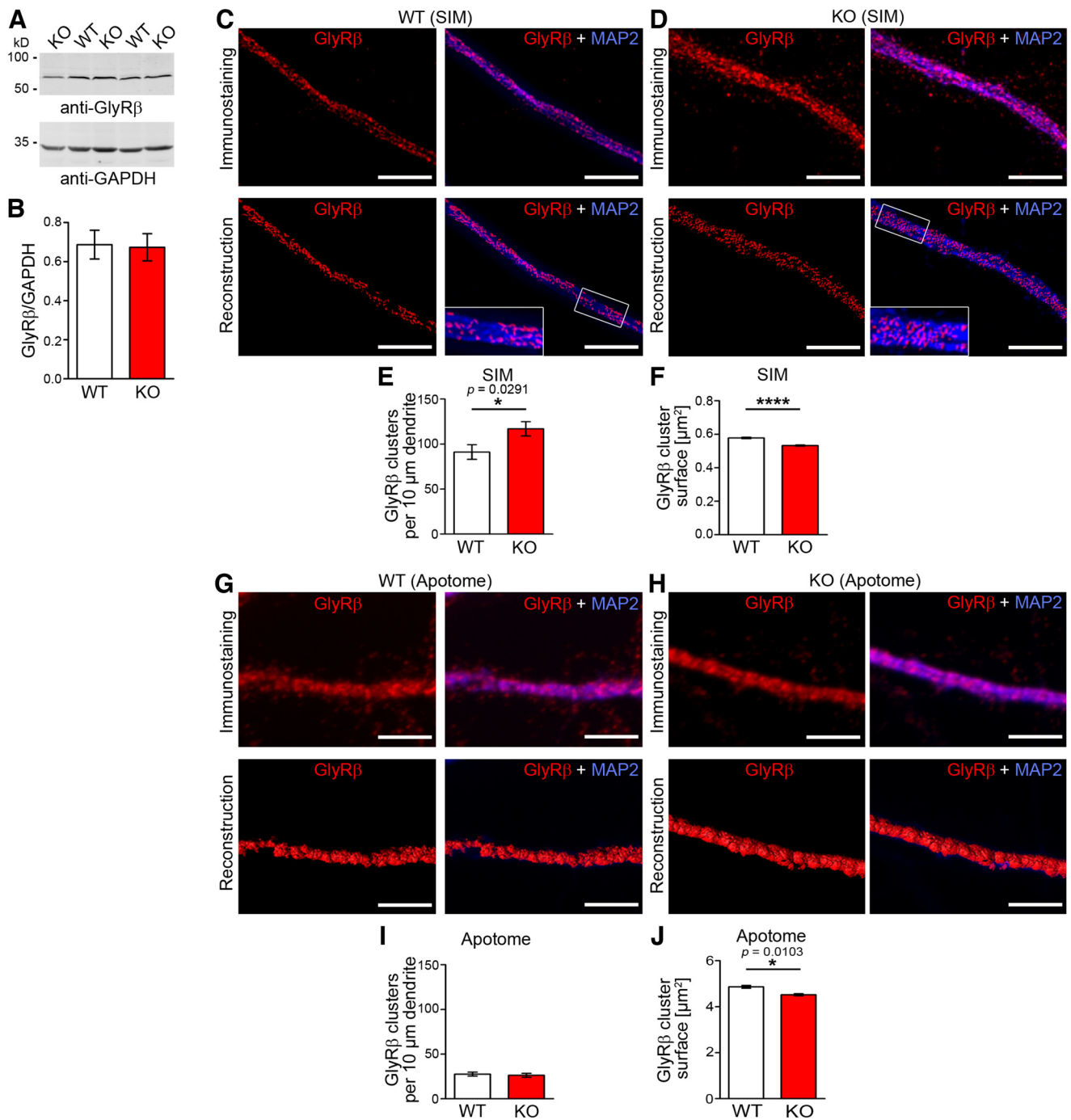


**Figure 2.** High-resolution immunofluorescence analyses unveil an increased abundance and a decreased size of GlyRβ clusters in *syndapin 1* KO spinal cord neurons. **A, B**, Quantitative immunoblotting analyses of GlyRβ expression levels in WT and *syndapin 1* KO spinal cord homogenates (normalized to anti-GAPDH levels; homogenates of  $n = 10$  mice/genotype; not significant). **C–J**, Analyses of GlyRβ clusters along dendrites of spinal cord neurons (DIV21/DIV22) from WT (**C,G**) and *syndapin 1* KO mice (**D,H**). Shown are SIM (**C,D**) and Apotome (**G,H**) immunofluorescence images of GlyRβ clusters (left top panels) and corresponding 3D reconstructions of GlyRβ clusters (red) (left bottom panels). Right panels represent merges with additional anti-MAP2 immunostaining and reconstructions, respectively, highlighting the dendritic areas (blue). Insets, Magnifications of boxed areas. Scale bars, 3 μm. Quantitative analyses of anti-GlyRβ cluster densities (**E,I**) and sizes (**F,J**). Data are mean ± SEM shown as bar plots. **E, I**,  $n = 20$  each (SIM) and  $n = 34/36$  (WT/KO) (Apotome) dendrite segments and cells per genotype of three independent preparations of primary neuronal cultures from several ( $\geq 3$ ) (pooled) E14 embryos.  $p = 0.0291$  (**E**) and not significant (**I**), respectively. **F, J**,  $n = 10184/12855$  (WT/KO) (**F**) and 7144/7234 (WT/KO) (**J**) GlyRβ clusters.  $****p < 0.0001$  (**F**) and  $*p = 0.0103$ , (**J**), respectively. Unpaired Student's  $t$  test (**B,E,I**); Mann–Whitney (**F,J**). For numerical data, see Extended Data Figure 2–1.

before by a more classical technique not providing such a high resolution (Apotome 3D imaging) (Fig. 2G,H). Strikingly, conventional immunofluorescence microscopy images of the same samples failed to resolve the increased density of GlyRβ clusters but led to results different from our SIM analyses. First, the absolute number of detected GlyRβ clusters was much lower than with SIM. Less than

one-third of the number of all SIM-detected clusters were detected (Fig. 2I). Second, also the increase in GlyRβ cluster density in *syndapin 1* KO neurons was not detected by conventional immunofluorescence microscopy (Fig. 2I; not significant).

Thus, in line with the small dimensions of inhibitory post-synapses in spinal cord neurons (Specht et al., 2013), our

evaluations demonstrated that conventional light microscopy was hampered by resolution limits. *Syndapin I* KO does not lead to GlyR $\beta$  cluster losses (del Pino et al., 2014) but results in a significant increase of GlyR $\beta$  cluster density (Fig. 2C–E;  $p = 0.0291$ ).

We next asked whether the SIM-based observation indicating that the increase in GlyR $\beta$  cluster density along dendrites, which came at the expense of GlyR $\beta$  cluster size (Fig. 2F;  $p < 0.0001$ ), would consistently also be seen by examinations of the same samples by conventional light microscopy. In line with reported increases of microscopic resolution by SIM (Gustafsson, 2005), the surfaces of GlyR $\beta$  clusters resolvable by the two methods differed by about one order of magnitude: for example, WT:  $0.6 \mu\text{m}^2$  (SIM) vs  $4.8 \mu\text{m}^2$  (Apotome). Yet, both methods consistently revealed that GlyR $\beta$  clusters surfaces in *syndapin I* KO neurons were significantly smaller than those in WT neurons (Fig. 2F,J;  $p < 0.0001$  and  $p = 0.0103$ , respectively).

Together, these results suggested a critical role of syndapin I in organizing GlyR $\beta$  arrays. Its function thereby seemed somewhat related to that of gephyrin.

### Quantitative ultrahigh-resolution analysis shows that *syndapin I* KO spinal cords have fragmented GlyR fields and a higher abundance of dispersely localized GlyR $\beta$ s

Even the increased resolution of SIM may still fail to detect even smaller GlyR clusters or single, dispersed GlyRs, which could putatively also occur due to *syndapin I* KO. EM allows for resolutions of better than 1 nm (i.e., can in principle resolve single proteins or even domains thereof). Receptor field examinations free from rotational artifacts would require undisturbed perpendicular views onto the plasma membrane (Seemann et al., 2017). Although to our knowledge never attempted thus far, let alone directly in spinal cord tissue, this could in principle be accomplished via plasma membrane freeze-fracturing and subsequent anti-GlyR $\beta$  immunogold labeling. We finally were indeed able (1) to freeze-fracture murine spinal cord tissue and (2) to furthermore label the resulting P-faces (cytosolic faces) of the freeze-fracture replica with anti-GlyR $\beta$  antibodies directed against cytosolic GlyR $\beta$  epitopes in a specific manner (Fig. 3A–D).

In WT spinal cords, GlyR fields were visualized by strikingly high densities of anti-GlyR $\beta$  immunogold labels, if small enough colloidal gold was used. Some receptor fields showed more irregular shapes, but many were relatively round and had diameters of  $\sim 150$  nm (Fig. 3C). Double immunogold labeling attempts to also visualize syndapin I failed under the conditions suitable for GlyR $\beta$  labeling. Both ice surfaces, but also the E-faces of fractured membranes, were devoid of anti-GlyR $\beta$  labeling (Fig. 3A,B). This demonstrated the specificity of the anti-GlyR $\beta$  immunolabeling.

*Syndapin I* KO spinal cords also displayed GlyR $\beta$  fields of relatively circular shapes. Strikingly, our ultrastructural imaging resolved that *syndapin I* KO GlyR $\beta$  clusters ( $\geq 3$  gold particles in  $< 50$  nm proximity) were only about half the size of those observed in WT tissue (Fig. 3C–E;  $p < 0.0001$ ). As the anti-GlyR $\beta$  immunogold labeling density within the cluster areas (Fig. 3F; not significant) and also the overall anti-GlyR $\beta$  immunogold labeling density at the plasma membrane showed no change in *syndapin I* KO spinal cords (Fig. 3G; not significant), no plasma membrane-bound GlyR $\beta$ s was lacking. Instead, the GlyR $\beta$ s distribution differed. *Syndapin I* KO spinal cords showed a  $> 50\%$  higher GlyR $\beta$  cluster density compared with WT (Fig. 3H;  $p = 0.0475$ ).

Additionally, non-clustered, that is, dispersed GlyR $\beta$  immunolabelings (i.e., single, double immunolabelings outside of any cluster) were much more abundant. The density of dispersed GlyR $\beta$  immunolabeling in *syndapin I* KO spinal cords was more than twice as high as in WT spinal cords (Fig. 3I;  $p = 0.0044$ ). Also, distribution analyses of all labels observed unveiled that *syndapin I* KO spinal cords displayed a strong increase in the percentage of dispersed GlyR $\beta$ s (Fig. 3J).

*Syndapin I* thus clearly plays a scaffolding role holding together GlyR $\beta$  fields. This finding was unexpected, as gephyrin is considered as the scaffold ensuring efficient GlyR $\beta$  clustering. Instead, it seemed that syndapin I and gephyrin cooperate in receptor scaffolding functions in a non-redundant manner, i.e., that also syndapin I plays an important role in holding together GlyR $\beta$  fields.

### Particularly small GlyR $\beta$ clusters in *syndapin I* KO spinal cord neurons lack the postsynaptic scaffold gephyrin

We next asked whether the fragmented and/or shrunken GlyR $\beta$  clusters in *syndapin I* KO mice still contain the postsynaptic scaffold gephyrin. Given the partial steric hindrances between gephyrin and syndapin I binding to GlyR $\beta$  (Fig. 1C), it even seemed likely that gephyrin may take over some of the docking sites of its GlyR $\beta$  binding neighbor syndapin I when syndapin I is knocked out. To our surprise, this was not the case. Quantitative analyses of gephyrin clusters by SIM (Fig. 4A,B) showed that the gephyrin cluster density (Fig. 4C) did not fully mirror the significant increase in GlyR $\beta$  cluster abundance (compare Fig. 2E, 27% and Fig. 3H, 50%). While also gephyrin clusters were significantly smaller in *syndapin I* KO spinal cord neurons (Fig. 4D;  $p < 0.0001$ ), their density only showed moderately increased values that failed to reach statistical significance despite high  $n$  numbers of dendritic segments analyzed (Fig. 4C; not significant). A simple explanation for the reduction of the gephyrin cluster sizes (Fig. 4D;  $p < 0.0001$ ) was that gephyrin expression levels may be reduced in *syndapin I* KO mice. Quantitative immunoblotting analyses, however, showed that gephyrin levels were similar in WT and *syndapin I* KO spinal cords (Fig. 4E,F; not significant).

An alternative explanation was that a subpopulation of GlyR $\beta$  clusters in *syndapin I* KO neurons is devoid of detectable gephyrin and that therefore the cluster density did not seem to increase in accordance with receptor field fragmentation. We therefore analyzed the gephyrin clusters in direct relation to coimmunostained GlyR $\beta$  clusters (Fig. 4G,H). Quantitative analyses of anti-gephyrin immunolabeling densities inside of GlyR $\beta$  clusters indeed demonstrated a reduction of the average anti-gephyrin immunolabeling intensity in GlyR $\beta$  clusters in *syndapin I* KO spinal cord neurons (Fig. 4I;  $p = 0.0295$ ). Interestingly, whereas large GlyR $\beta$  clusters in *syndapin I* KO neurons even showed an increase in mean anti-gephyrin labeling intensity compared with WT (Fig. 4J; 4.6%;  $p = 0.0018$ ), which could reflect an additional incorporation of gephyrins into receptor scaffolds in the absence of syndapin I, the gephyrin intensity reduction in GlyR $\beta$  clusters of *syndapin I* KO neurons in particular occurred in GlyR $\beta$  clusters that were smaller or equal to the mean surface of GlyR clusters (including SD, i.e.,  $\leq 0.9929 \mu\text{m}^2$ ) (Fig. 4K;  $-12\%$ ;  $p = 0.0190$ ). Consistently, the rare fraction of GlyR clusters that were completely negative for any anti-gephyrin immunostaining also appeared higher in *Syndapin I* KO neurons compared with WT neurons (Fig. 4L).

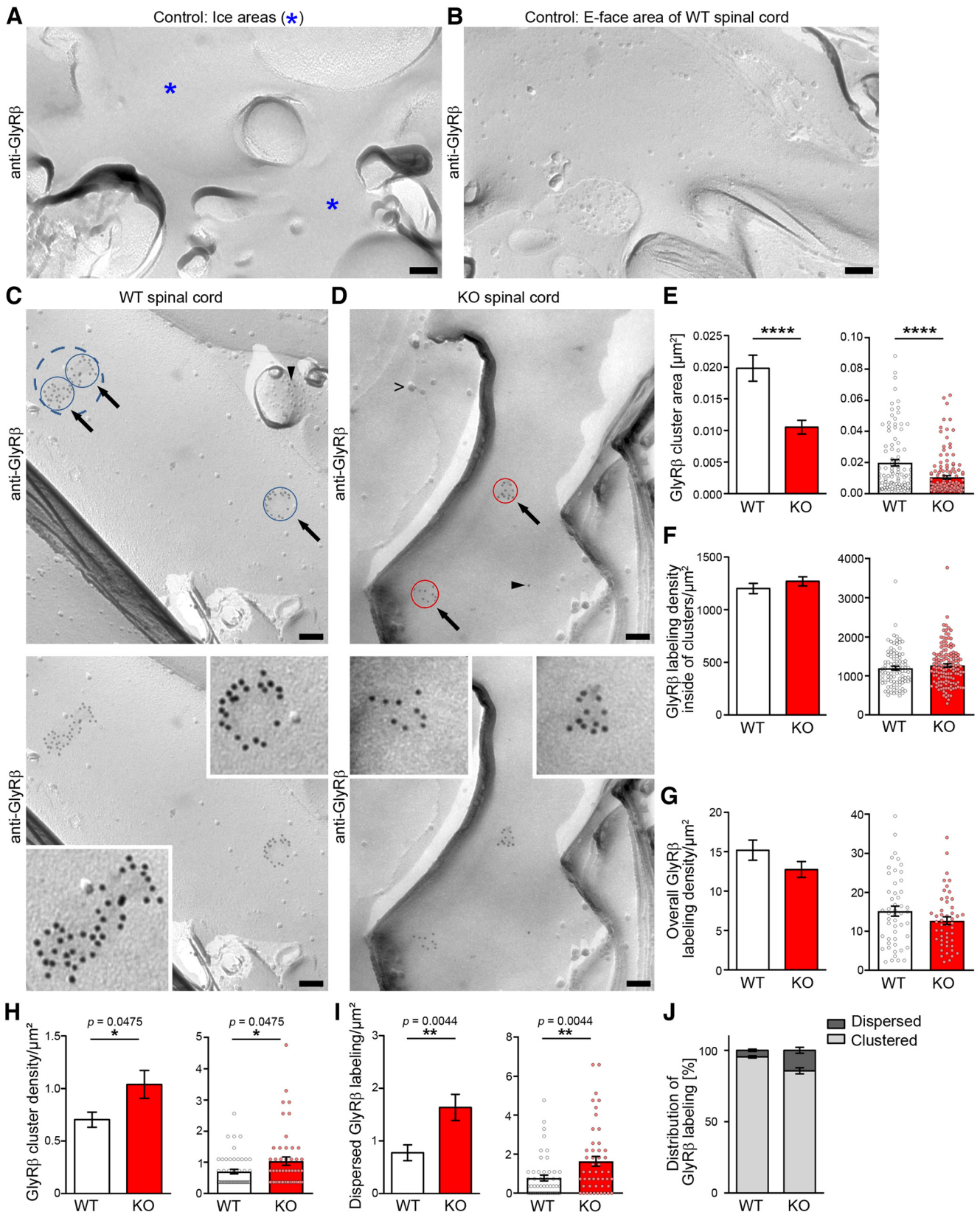


**Figure 3.** Electron microscopic analyses of immunogold labeled freeze-fracture replica of spinal cords unveil an increased abundance and defects in organization of GlyR $\beta$  clusters in *syndapin 1* KO spinal cords. **A, B**, TEM images of freeze-fractured spinal cord plasma membranes from WT (**A–C**) and *syndapin 1* KO mice (**D**) labeled with immunogold conjugates directed against the intracellular loop of the GlyR $\beta$  (pointed out by arrows) and specificity controls thereof (**A**, WT, ice areas and **B**, WT, E-face areas). The GlyR $\beta$  clusters detected are larger in WT (**C**; clusters are encircled in blue; an alternative consideration [large cluster instead of two adjacent ones] is encircled by a dashed line) than in *syndapin 1* KO specimen (**D**; clusters encircled in red). Arrowheads indicate dispersed GlyR $\beta$  immunogold labelings (1 and 2 gold particles). Bottom panels, The above TEM images without any putatively covering labeling. Insets, The GlyR $\beta$  clusters at enhanced magnification and increased contrast. Scale bars (**A–D**), 100 nm. **E–J**, Quantitative analyses of GlyR $\beta$  immunolabeling at the plasma membrane in WT and *syndapin 1* KO



These results for the small GlyR $\beta$  clusters in *syndapin I* KO neurons were stunning. The observed partial competition of gephyrin and syndapin I for binding to the cytoplasmic loop of the GlyR receptor should rather allow for an improved gephyrin binding by *syndapin I* KO. Yet, the opposite was observed. A subpopulation of GlyR $\beta$  clusters in *syndapin I* KO spinal cords had lost some gephyrin, and this subpopulation corresponded to the small clusters that occurred with higher abundance in *syndapin I* KO neurons.

### Syndapin I deficiency leads to an increased mobility of GlyR $\beta$ clusters

To shed some more light on syndapin I's crucial role in GlyR $\beta$  scaffolding, we next asked whether syndapin I might contribute to synaptic GlyR $\beta$  immobilization. Upon syndapin I knockdown in rat spinal cord neurons, both the spot mobility and the displacement length of GFP-GlyR $\beta$  were significantly increased compared with control (Fig. 5A–D). The maximal velocity of tracked GFP-GlyR $\beta$  spots increased by 15% in syndapin I-deficient neurons (Fig. 5C). Additionally, the mean displacement length of tracked clusters increased by ~50% in syndapin I-deficient neurons (Fig. 5D). Both defects observed in syndapin I-deficient neurons were highly statistically significant compared with WT and thus clearly represented syndapin I loss-of-function phenotypes in receptor anchoring (Fig. 5C,D; both  $p < 0.0001$ ).

### Syndapin I KO completely disrupts the kainate-induced internalization of GlyR

Biochemically, we did not only observe cooperative functions of gephyrin and syndapin I but also some competition for GlyR $\beta$  (Fig. 1). While the defects in receptor organization observed in *syndapin I* KO samples (Figs. 2–5) pointed to some scaffolding role of syndapin I, which was somewhat cooperative but not redundant with gephyrin, there furthermore should be functions of syndapin I, which are promoted by the absence of gephyrin association, and thereby rather reflect the competitive behavior of gephyrin and syndapin I. In recent years, it has been shown that certain conditions lead to detectable GlyR endocytosis. PKC-induced GlyR endocytosis has been shown in GlyR-overexpressing in HEK293 cells (Huang et al., 2007; Breitingner et al., 2018). Importantly, finally also the endogenous receptors in cultures of dissociated spinal cord neurons were shown to be internalized when PKC was activated via stimulating the neurons with kainate (Sun et al., 2014). The mechanisms of GlyR endocytosis and how the to-be-internalized receptors could be decoupled from the extended postsynaptic gephyrin-based scaffold holding together the large receptor fields largely remained elusive. This prompted us to hypothesize that syndapin I could represent a critical player in this process and may be involved in a molecular

switching mechanism between receptor anchoring and scaffolding on one side and receptor endocytosis on the other side. Using antibody internalization assays based on the same pan-anti-GlyR antibody as published (Sun et al., 2014), we were able to reproduce the finding that almost 30% of the GlyRs were internalized when WT neurons were incubated with kainate (Fig. 6A–C;  $p = 0.0035$ ).

Intriguingly, *syndapin I* KO completely abolished this kainate-induced GlyR endocytosis in cultures of spinal cord neurons (Fig. 6D–F). The rates of cell surface-localized to internalized endogenous GlyR in *syndapin I* KO neurons did not show any response to kainate stimulation at all (Fig. 6F; not significant).

These experiments thus identify syndapin I as a critical component for kainate signaling-induced endocytosis of GlyRs in spinal cord neurons and that this cellular function is independent of proper integration of the neurons into the spinal cord tissue but also occurs in dissociated, cultured neurons.

### Ultrahigh-resolution analyses demonstrate a disruption of the kainate-induced removal of GlyR $\beta$ from the plasma membrane in dissociated, cultured spinal cord neurons from *syndapin I* KO mice

In order to examine the removal of GlyR $\beta$ s from the plasma membrane of spinal cord neurons at ultrahigh-resolution using EM, we set up cultures of dissociated neurons from spinal cords of WT and *syndapin I* KO mice, respectively, on sapphire discs suitable for freeze-fracturing and again used the kainate stimulation conditions previously used to establish kainate-driven changes of GlyR surface availability in cultured cells (Sun et al., 2014). Under the cell culture conditions used, the primary cells polarized normally and formed elongated axons and dendrites during the first days in culture on sapphire (Fig. 7A). After about 2 more weeks, the primary mouse spinal cord neurons also had formed synapses (Fig. 7B). We indeed succeeded in cryopreserving and freeze-fracturing the fragile networks of cultured spinal cord neurons. This, for the first time, allowed us to move examinations of GlyR reorganization in cultured spinal cord neurons to the ultrahigh-resolution level of quantitative EM (Fig. 7C–F).

The cultured spinal cord neurons showed a significant removal of GlyR $\beta$  from the plasma membrane of WT cultured spinal cord neurons after 1 min of treatment with 200  $\mu$ M kainate and 10 min postincubation in medium (Fig. 7C,D). Quantitative analyses unveiled that almost one-third of all GlyR $\beta$  was removed from the plasma membrane of WT neurons after the kainate stimulation (Fig. 7G,H;  $p = 0.0008$  and  $p = 0.0390$ , respectively).

Importantly, the kainate-driven removal of GlyR $\beta$  from the plasma membrane was disrupted when freeze-fractured spinal cord neurons from *syndapin I* KO mice were examined by EM (Fig. 7E,F). Highlighting the importance of syndapin I for kainate-induced GlyR $\beta$  rearrangements, the anti-GlyR $\beta$  immunogold labeling density of plasma membranes of the kainate-stimulated spinal cord neurons in the *syndapin I* KO group remained at control level (Fig. 7H; not significant).

### Kainate-induced GlyR $\beta$ removal from the plasma membrane can also be demonstrated in spinal cords

It remained to be addressed whether the internalization of GlyR in WT neuronal cultures induced by incubation with 200  $\mu$ M kainate for 1 min (Sun et al., 2014; present study) (Figs. 6, 7) also occurs in intact spinal cords. Also, it is a pressing question, which

←

samples of spinal cords, including determinations of the GlyR $\beta$  cluster sizes (E), the labeling density within receptor fields (F), the density of membrane-bound anti-GlyR $\beta$  immunolabeling in total (G), the density of GlyR $\beta$  clusters (H), the density of dispersed anti-GlyR $\beta$  immunolabeling (I), and the distribution of anti-GlyR $\beta$  immunogold labeling between clustered and dispersed (J). E–J, Data are mean  $\pm$  SEM, shown as bar plots at the left and bar/dot plot presentations at the right. J, Data distribution analysis shown as cumulative column representation. E–J,  $n = 50/49$  (WT/KO) images for density determinations and  $n = 96/139$  (WT/KO) individual GlyR $\beta$  clusters (representing all clusters found in the 50/49 (WT/KO) images). Data were recorded from two independent spinal cord preparations. Mann–Whitney (E–I). \*\*\*\* $p < 0.0001$  (E); not significant (F,G); \* $p = 0.0475$  (H); and \*\* $p = 0.0044$  (I), respectively. For numerical data, see Extended Data Figure 3-1.

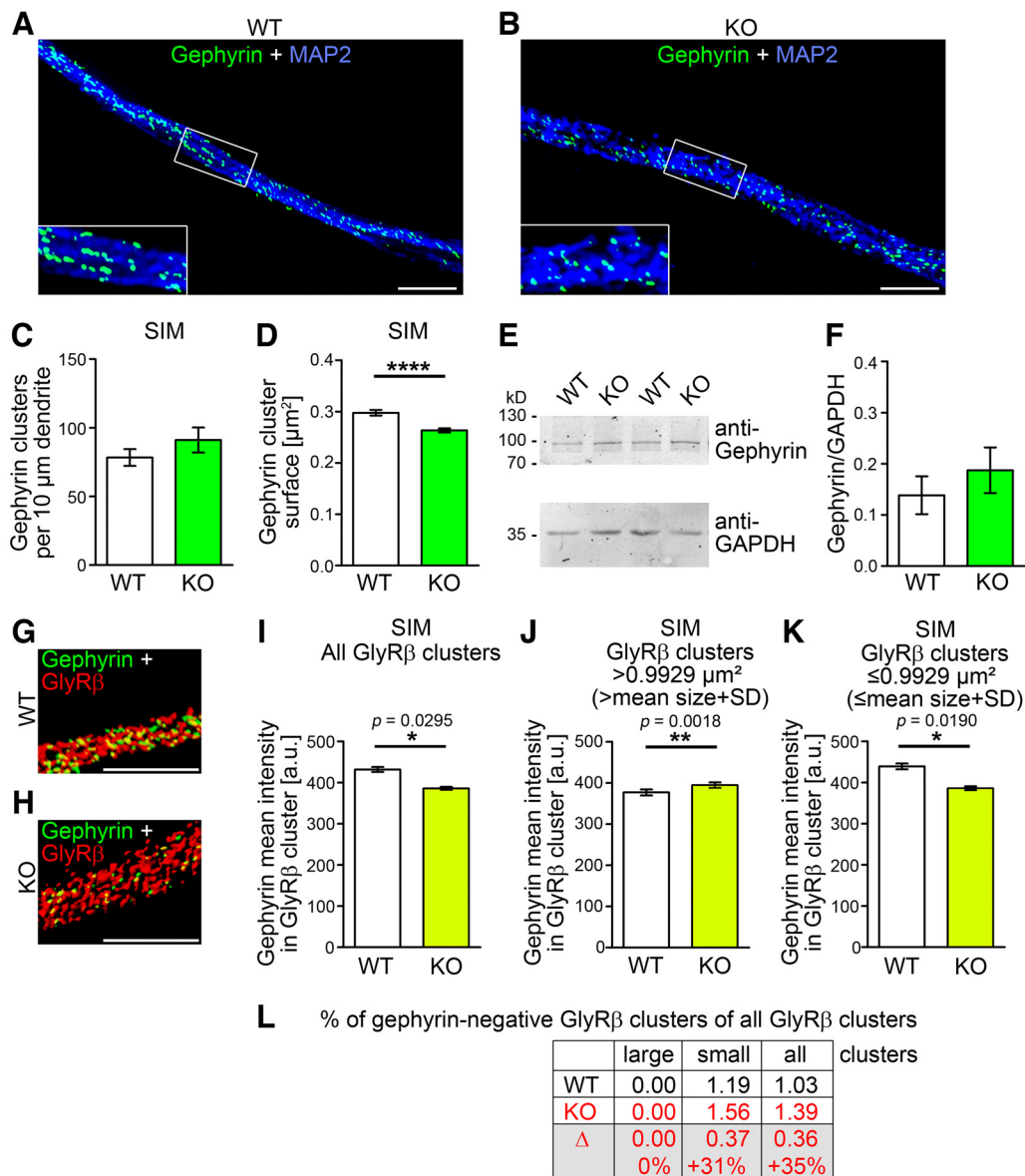


**Figure 4.** *Syndapin 1* KO specifically reduces gephyrin clusters sizes in small GlyR $\beta$  clusters. **A–D**, 3D reconstructions of anti-gephyrin clusters in anti-MAP2-labeled dendrites of neurons (DIV21/DIV22) isolated at E14 from WT (**A**) and *syndapin 1* KO spinal cords (**B**) using SIM and quantitative analyses of the gephyrin cluster density along dendrites (**C**) and of the sizes of the gephyrin clusters (**D**). Insets, Magnifications of boxed areas. Scale bars, 3  $\mu$ m. **E, F**, Quantitative immunoblotting analyses of gephyrin expression levels in WT and *syndapin 1* KO spinal cord homogenates (normalized to anti-GAPDH levels). **G–K**, Quantitative analyses of mean anti-gephyrin intensities in GlyR $\beta$  clusters in dendrites of DIV21/DIV22 spinal cord neurons isolated from WT and *syndapin 1* KO spinal cords. Anti-gephyrin and anti-GlyR $\beta$  immunolabeled neurons were imaged by SIM (**G,H**). Scale bars, 3  $\mu$ m. The mean anti-gephyrin intensities are shown regardless of the corresponding GlyR $\beta$  cluster size (**I**) as well as separately in larger (**J**) and in GlyR $\beta$  clusters equal to and smaller (**K**) than the average WT GlyR $\beta$  cluster size (expressed as cluster surface of 3D-reconstructed GlyR $\beta$  clusters (0.5777  $\mu$ m<sup>2</sup> + SD (0.4152  $\mu$ m<sup>2</sup>), i.e.,  $\leq$ 0.9929  $\mu$ m<sup>2</sup>). **L**, Fraction of rare cases of completely gephyrin-negative GlyR $\beta$  clusters in WT and *syndapin 1* KO neurons in percent of total. **C, D, F, I–K**, Data are mean  $\pm$  SEM, shown as bar plots. **C**,  $n = 21$  (WT) and 23 (KO) dendritic segments and cells recorded from two independent neuronal preparations. **D**, 9372/11982 (WT/KO) gephyrin clusters (representing all clusters in the 21/23 (WT/KO) images of dendritic segments). **E, F**,  $N = 10$  mice/genotype. **I–K**,  $n = 10184/12855$  (WT/KO) (**I**), 1397/1389 (WT/KO) (**J**), and 8787/11466 (WT/KO) (**K**) gephyrin clusters from 20 cells each from three independent preparations from 3 + 8 + 8 WT pooled embryos and 4 + 3 + 11 pooled KO embryos, respectively. Unpaired Student's *t* test (**C**; not significant) and Mann–Whitney (**D,F,I–K**), respectively. \*\*\*\* $p < 0.0001$  (**D**); not significant (**F**); \* $p = 0.0295$  (**I**); \*\* $p = 0.0018$  (**J**); and \* $p = 0.0190$  (**K**), respectively. For numerical data, see Extended Data Figure 4-1.

types of changes in receptor field organization bring about this form of receptor and synapse modulation.

Compared with cultured, dissociated spinal cord neurons, neurons embedded into the tissue are much less accessible. In order to increase the chance of full tissue penetration, we applied 1 mM kainate for 1 h. It was shown that 1 mM kainate applied for 1 h did not cause any neuronal death in spinal cords but that detectable neuronal death required 1 d and longer to develop (Taccola et al., 2008; Kuzhandaivel et al., 2010). Even pyknosis was not observed at 1 mM kainate applied for 1 h (Kuzhandaivel

et al., 2010). Thus, the conditions used were suitable to avoid any potential disintegration of GlyRs and data artifacts caused by excitotoxicity. Since, furthermore, the (in part minor) pyknosis effects that eventually were detectable after much more prolonged kainate incubations of spinal cords were mostly found at the dorsal side and delayed minor effects also occurred centrally, we took all of our spinal cord samples from the ventral side. The ventral side of the spinal cord did not even show pyknosis after incubation with 1 mM kainate for an entire day (Kuzhandaivel et al., 2010).

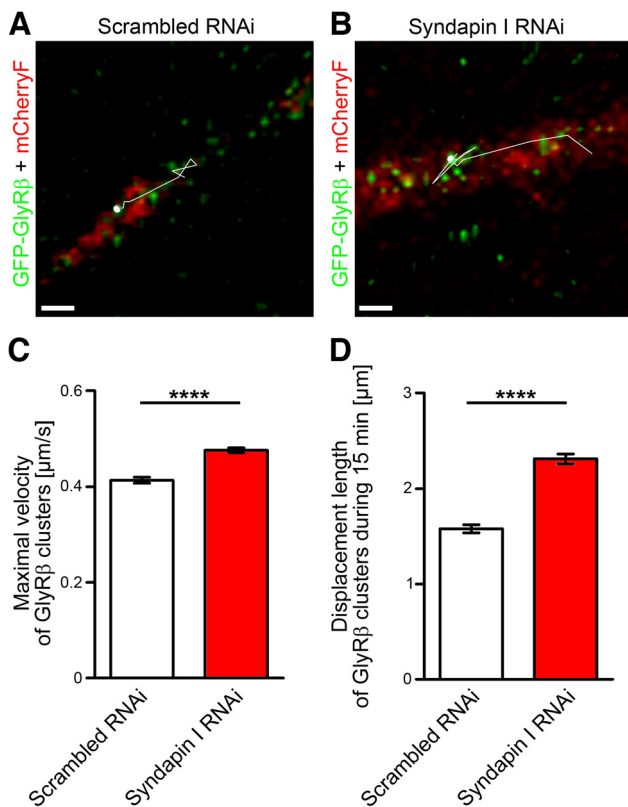


**Figure 5.** Syndapin I deficiency leads to an increased mobility of GFP-GlyR $\beta$  clusters. **A, B**, Examples of trajectories from reconstructed GFP-GlyR $\beta$  clusters projected onto merged images of rat spinal cord neurons double-transfected with GFP-GlyR $\beta$  (green) and scrambled RNAi/mCherryF (red) (**A**) and with GFP-GlyR $\beta$  and syndapin I RNAi/mCherryF (**B**), respectively. Spheres represent the respective start point of the GFP-GlyR $\beta$  tracking. Scale bar, 1  $\mu$ m. **C, D**, Quantitative analyses of GFP-GlyR $\beta$  cluster speeds (**C**) and displacement lengths (**D**) in spinal cord neurons cotransfected with either syndapin I RNAi and control (scrambled RNAi) plasmids and imaged by spinning disc microscopy. Data are mean  $\pm$  SEM.  $n = 1634$  tracks from 10 neurons (scrambled RNAi) and 2251 tracks from 11 neurons (syndapin I RNAi). Mann–Whitney, \*\*\*\* $p < 0.0001$  (**C, D**). For numerical data, see Extended Data Figure 5-1.

Demonstrating the physiological importance of the kainate-induced GlyR removal from the plasma membrane established in dissociated neurons, we were indeed able to show that freeze-fracture replica of intact spinal cord tissue of WT mice revealed a substantial decline of general GlyR $\beta$  labeling density when treated with 1 mM kainate for 60 min (Fig. 8A). These results firmly demonstrated at ultrahigh-resolution that kainate-induced internalization of GlyR $\beta$  also occurs at the spinal cord tissue level.

Strikingly, even incubations with only 200  $\mu$ M kainate used to establish kainate-induced GlyR rearrangements in dissociated spinal cord neurons (Sun et al., 2014) for merely 10 min in total allowed for sufficient tissue penetration to give rise to strong GlyR $\beta$  rearrangements in spinal cords (Fig. 8B–F) that very closely mirrored those seen before with the 1 h treatment of spinal cords (Fig. 8A). Also, the much shorter incubation of the spinal cord specimen with the lower kainate concentration led to a reduction of the GlyR $\beta$  labeling density at the plasma membrane by about one-third (Fig. 8F; WT,  $p = 0.0007$ ). Even in spinal cord tissue, the removal of GlyR $\beta$  from the plasma membrane thus seems to be a rather quick ( $\leq 10$  min) neuronal response to kainate.

### Kainate-treated spinal cords of *syndapin I* KO mice show impaired GlyR $\beta$ uptake

Syndapin I deficiency led to an impairment of kainate-induced GlyR $\beta$  internalization in dissociated neurons (Figs. 6, 7). Similarly, a complete disruption of GlyR $\beta$  removal from the plasma membrane was observed in spinal cords of *syndapin I* KO mice when the tissue samples were incubated with 1 mM kainate for 1 h. In contrast to WT, the overall density of GlyR $\beta$  at the plasma membrane of *syndapin I* KO spinal cords did not decline at all when subjected to stimulation by kainate (Fig. 8A; KO, not significant;  $13 \pm 1/\mu\text{m}^2$  (control) vs  $14 \pm 1/\mu\text{m}^2$  (kainate)).

A complete disruption of kainate-induced GlyR $\beta$  was also observed when *syndapin I* KO spinal cords were incubated with 200  $\mu$ M kainate for only 10 min (Fig. 8D–F; KO, not significant).

The observation that *syndapin I* KO spinal cords did not show any decline of GlyR $\beta$  labeling densities at the plasma membrane when incubated with kainate using two conditions that both reliably induced kainate-induced GlyR $\beta$  removal from the plasma membrane in WT spinal cord samples demonstrated that kainate-induced GlyR $\beta$  removal from the plasma membrane critically depends on syndapin I.

### Kainate-treated spinal cords of *syndapin I* KO mice show a massive disruption of GlyR $\beta$ field organization

What may be the receptor reorganizations allowing for the kainate-induced disappearance of a significant proportion of GlyR $\beta$ s from the plasma membrane in WT spinal cords? It was conceivable that GlyR $\beta$  fields would become more loosely connected because of the kainate- and PKC-mediated decrease of gephyrin binding. We thus closely analyzed all individual GlyR clusters present in the EM pictures of freeze-fractured spinal cord samples for kainate-induced changes in WT and *syndapin I* KO spinal cords (Fig. 9A–D). Yet, in WT animals, we did not observe that receptor packaging inside of receptor fields showed any signs of decrease by kainate stimulation (Fig. 9E; WT, not significant). It thus appeared likely that receptor fields may simply break into smaller fragments in kainate-stimulated spinal cords. Yet, our quantitative analyses showed that the GlyR $\beta$  cluster density did not increase but again rather showed the opposite trend (Fig. 9F; WT, not significant).

How then do  $>25\%$  of all GlyR $\beta$ s (compare Fig. 8A) disappear from the plasma membrane when WT spinal cords are incubated with kainate? We thus next analyzed whether individual receptors may leave the receptor fields. As the overall packaging of receptors within the fields was unchanged, such a mechanism should manifest in smaller receptor field areas and in an increase of dispersed GlyR $\beta$  immunolabeling at the plasma membrane. Indeed, we observed a  $\sim 25\%$  decline in WT GlyR $\beta$  cluster size by kainate treatment compared with control incubations of WT spinal cords (Fig. 9G; WT,  $p = 0.0251$ ). In contrast, a statistically significant increase of GlyR $\beta$ s localized in a dispersed manner in the plasma membrane was not observed (Fig. 9H; WT, not significant).

We thus concluded that the reorganizations of the receptor fields subsequent to kainate stimulation in WT spinal cords mostly involve a shrinkage of receptor fields and that receptors or small clusters of receptors removed from the receptor fields largely do not remain at the plasma membrane of WT spinal cords.

The lack of any change in GlyR $\beta$  density at the plasma membrane of *syndapin I* KO neurons may imply that there is no kainate-induced GlyR $\beta$  rearrangement in *syndapin I* KO neurons. Strikingly, however, ultrahigh-resolution analyses of GlyR $\beta$  at

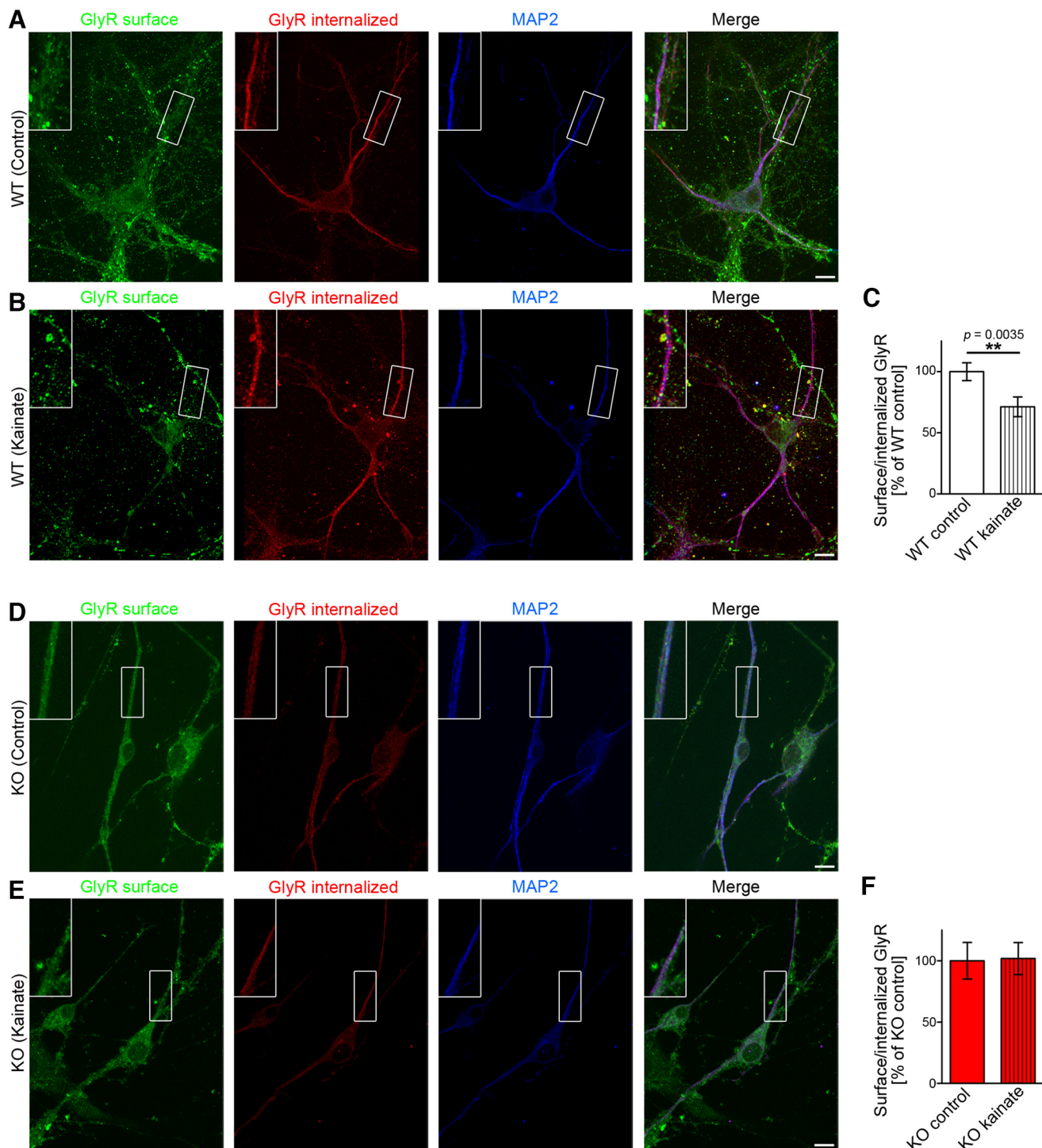


**Figure 6.** Syndapin I is crucial for GlyR endocytosis. **A, B, D, E**, MIPs of single channels and merged immunofluorescence images (Apotome; 0.3  $\mu\text{m}$  intervals) of surface GlyR (green), internalized GlyR (red), and MAP2 (blue) in anti-GlyR antibody internalization assays with WT (**A, B**) and *syndapin I* KO spinal cord neurons (DIV20/DIV21) (**D, E**) stimulated with 200  $\mu\text{M}$  kainate for 1 min followed by an incubation for 10 min to allow for GlyR internalization. Insets, Magnifications of boxed areas. Scale bars, 10  $\mu\text{m}$ . Quantitative analyses unveiling a full block of GlyR internalization by *syndapin I* KO (**C, F**). Data, mean  $\pm$  SEM of  $n = 66/46$  (WT control/kainate) (**C**) and 50/50 (KO control/kainate) (**F**) cells from three independent experiments and neuronal preparations each. Mann–Whitney,  $**p = 0.0035$  (**C**) and not significant (**F**), respectively. For numerical data, see Extended Data Figure 6-1.

the plasma membrane revealed that this was a misassumption. The anti-GlyR $\beta$  labeling density inside of GlyR $\beta$  clusters increased (Fig. 9E; KO,  $p = 0.0013$ ). Also, the density of GlyR $\beta$  clusters in *syndapin I* KO spinal cords, which was already elevated compared with WT (Fig. 3H), increased even further when kainate was added (Fig. 9F; KO,  $p = 0.0003$ ). Correspondingly, the size of GlyR $\beta$  clusters, which anyway already was strongly

reduced in *syndapin I* KO samples compared with WT (Fig. 3E), strongly decreased even further when the tissue was treated with kainate (Fig. 9G; KO,  $p = 0.0014$ ).

Interestingly, similar to the density of GlyR $\beta$  clusters (Fig. 9F), also the dispersed anti-GlyR $\beta$  immunolabeling in *syndapin I* KO spinal cords did not decline when the tissue was incubated with kainate. While it was  $\sim 0.8/\mu\text{m}^2$  in untreated WT and  $1.6/\mu\text{m}^2$

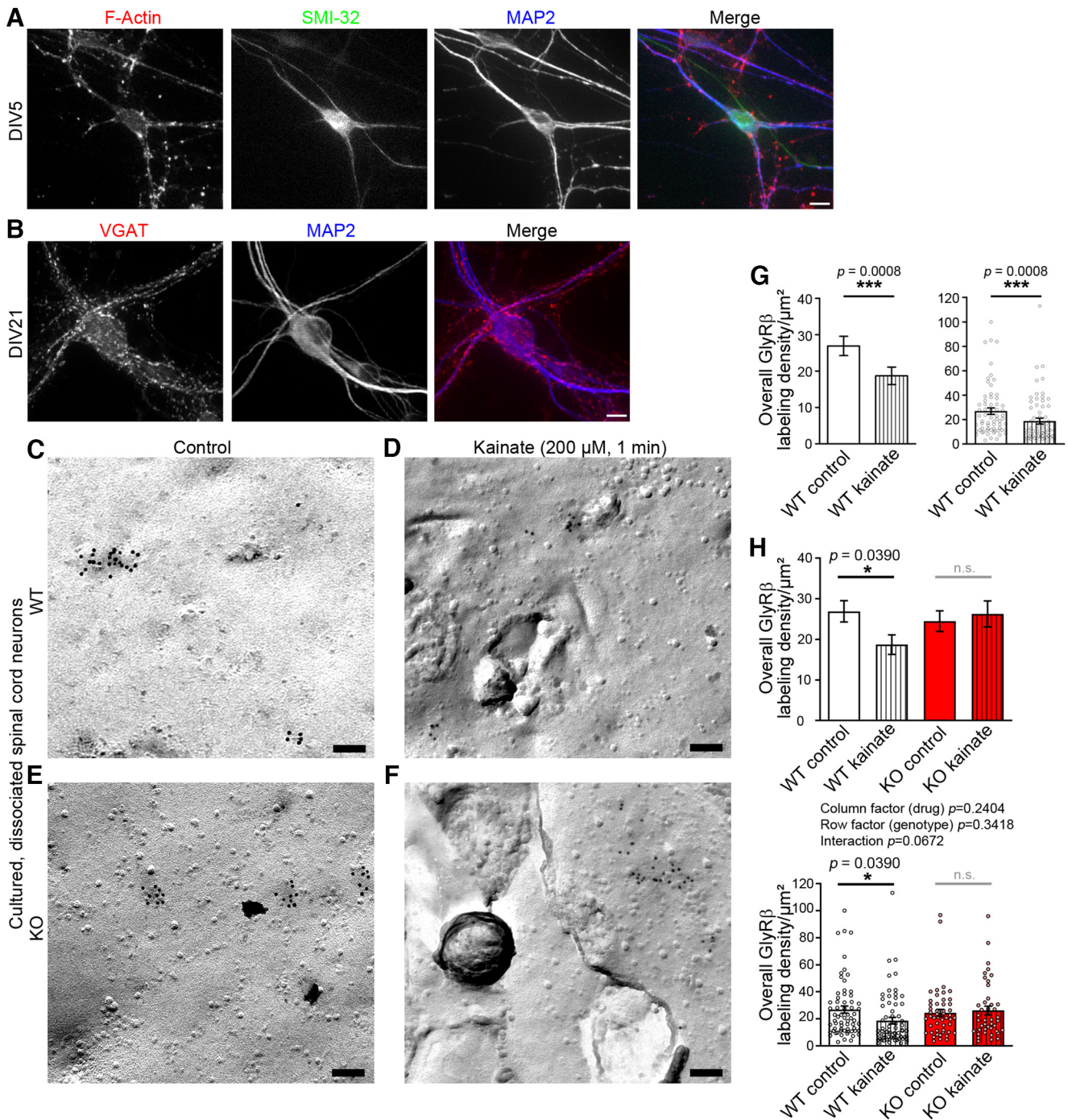


**Figure 7.** Kainate-induced removal of GlyR $\beta$  from the plasma membrane is observable in cultured, dissociated spinal cord neurons at the ultrahigh-resolution level using freeze-fracturing, immunogold labeling and TEM. **A, B**, MIP immunofluorescence images (Apotome; 0.3  $\mu\text{m}$  intervals) of WT spinal cord neurons grown on sapphire discs visualizing proper neuronal morphogenesis and network formation for two individual time points in culture. **A**, DIV5 spinal cord neurons incubated with phalloidin-488 to label F-actin (red) and with antibodies against the motor neuron marker SMI-32 (green) as well as with antibodies against the neuronal marker MAP2 (blue). **B**, DIV21 spinal cord neurons immunostained with antibodies against the presynaptic marker VGAT (red) and against the neuronal marker MAP2 (blue). Scale bars, 10  $\mu\text{m}$ . **C–F**, TEM images of anti-GlyR $\beta$  immunogold-labeled, freeze-fractured plasma membranes of DIV20/ DIV21 cultured, dissociated spinal cord neurons from WT (**C,D**) and *syndapin 1* KO mice (**E,F**), that either represented controls (**C,E**) or were treated with 200  $\mu\text{M}$  kainate for 1 min (**D,F**). Scale bars, 100 nm. **G, H**, Quantitative analyses of the overall GlyR $\beta$  immunolabeling densities in WT cultured spinal cord neurons (**G**) as well as WT versus KO comparisons (**H**). Data are mean  $\pm$  SEM, as bar plots optimally visualizing the differences of the mean and as bar/dot plots showing all individual data points (**G,H**).  $n = 65$  (WT control),  $n = 50$  (KO control),  $n = 66$  (WT kainate), and  $n = 42$  (KO kainate) images, respectively, from two independent preparations of primary spinal cord neurons from E14 mouse embryos. Mann–Whitney (**G**; \*\*\* $p = 0.0008$ ) and two-way-ANOVA and Bonferroni post-test for control versus kainate comparisons (**H**; WT, \* $p = 0.0390$ , and KO, not significant, respectively). For numerical data, see Extended Data Figure 7-1.

in untreated *syndapin 1* KO spinal cords, it rose to  $>2.5/\mu\text{m}^2$  when *syndapin 1* KO spinal cords were incubated with kainate, an increase of almost 60% compared with control *syndapin 1* KO spinal cord freeze-fractured membranes (Fig. 9H; KO,  $p = 0.0106$ ). In contrast,

in WT samples, the density of the dispersed GlyR $\beta$ s remained at very low levels ( $\sim 0.9/\mu\text{m}^2$ ) when treated with kainate and thereby resembled the values of untreated (control) spinal cords (Fig. 9H; not significant).

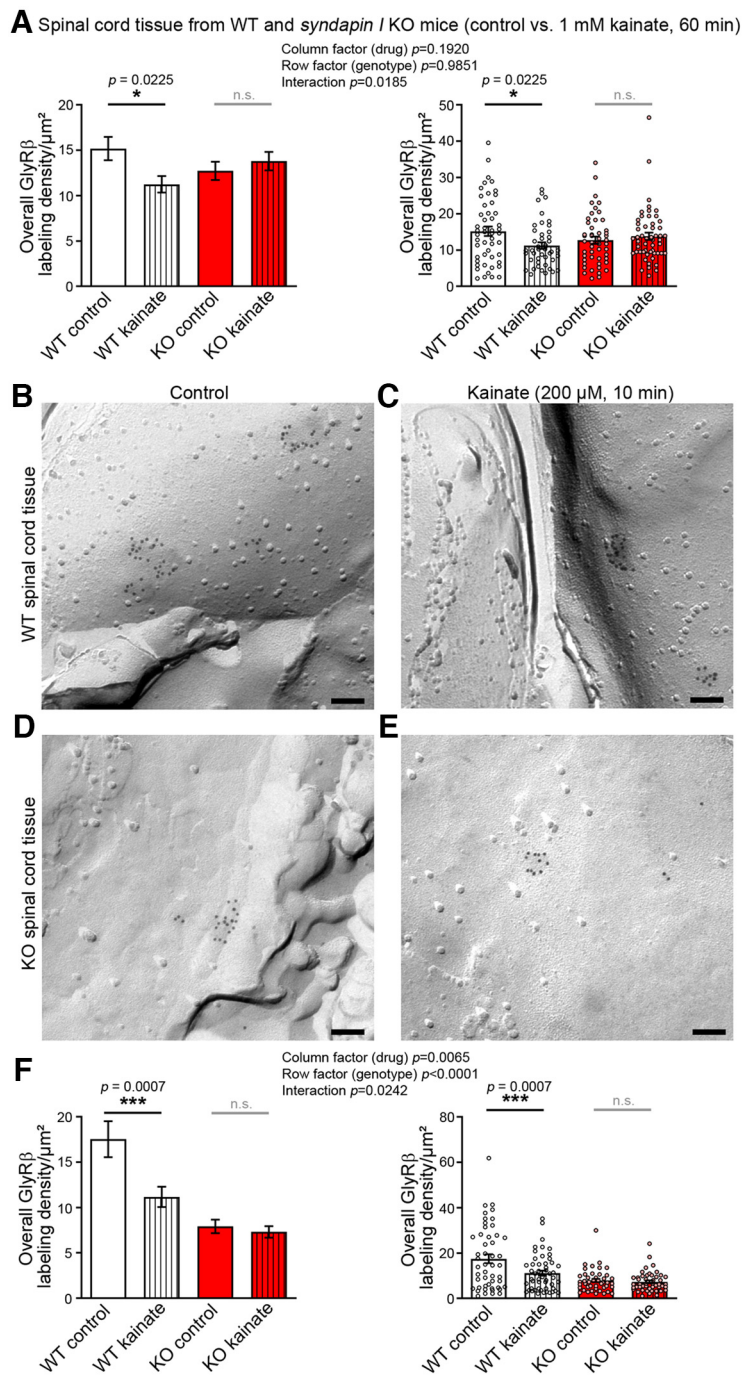


**Figure 8.** Kainate-induced GlyR $\beta$  removal from the plasma membrane demonstrated in WT spinal cords is completely impaired in *syndapin I* KO spinal cords. **A**, Quantitative analyses of the overall GlyR $\beta$  immunolabeling densities observed in TEM images of the plasma membrane of freeze-fractured WT and *syndapin I* KO spinal cords incubated with 1 mM kainate for 60 min. Data are mean  $\pm$  SEM shown as bar plots optimally visualizing the differences of the mean and as bar/dot plots showing all individual data points. **B–E**, TEM images of anti-GlyR $\beta$  immunogold-labeled, freeze-fractured spinal cords from adult WT (**B,C**) and *syndapin I* KO mice (**D,E**), that either represented controls (**B,D**) or were treated with 200  $\mu$ M kainate for 10 min (**C,E**; kainate). Scale bars, 100 nm. **F**, Quantitative analyses of the overall GlyR $\beta$  immunolabeling densities at the plasma membrane of freeze-fractured WT and *syndapin I* KO spinal cords. Data are mean  $\pm$  SEM shown as bar plots and as bar/dot plots: **A**,  $n=50$  (WT control, see also data Fig. 2),  $n=49$  (KO control, see also data Fig. 2),  $n=45$  (WT kainate), and  $n=53$  (KO kainate) images, and (**F**)  $n=49$  (WT control),  $n=45$  (KO control),  $n=51$  (WT kainate), and  $n=47$  (KO kainate) images, respectively, from two independent neuronal preparations. Two-way-ANOVA and Bonferroni post-test for control versus kainate comparisons (**A**, WT,  $*p=0.0225$ , and KO, not significant, respectively; **F**, WT,  $***p=0.0007$ , and KO, not significant, respectively). For numerical data, see Extended Data Figure 8-1.

Together, *syndapin I* KO spinal cords showed a massive reorganization of GlyR $\beta$  receptor organization at the plasma membrane when treated with kainate; whereas in WT samples, GlyR $\beta$  receptors or receptor aggregates decoupled from larger receptor fields disappear from the plasma membrane by internalization.

### The PKC-dependent phosphorylation site S403 of GlyR $\beta$ is an important switch for diminishing gephyrin binding and simultaneously promoting *syndapin I* association

Our quantitative TEM analyses unveiled that a lack of *syndapin I* disrupts GlyR $\beta$  removal from the plasma membrane. Furthermore, upon stimulation with kainate, *syndapin I* KO caused a strong fragmentation of receptor fields. This indicated that, without *syndapin I* and under the condition of kainate stimulation, gephyrin was unable to effectively scaffold receptor fields. Kainate induces PKC activity, and PKC phosphorylation of GlyR $\beta$  at S403 has been reported to cause a reduction of gephyrin binding (Specht et al., 2011). Receptor decoupling from the scaffold may therefore be one aspect in kainate-induced receptor dynamics and inhibitory synapse plasticity. However, our data show that WT receptor fields, to a large extent, nevertheless persist despite kainate incubation. Analyses of *syndapin I* KO spinal cords revealed that this persistence to a significant part depends on *syndapin I*. It thus seemed that *syndapin I*-mediated scaffolding is not negatively affected by GlyR $\beta$  S403 phosphorylation. Intriguingly, *syndapin I* binding to GlyR $\beta$  even turned out to be promoted by S403 phosphomimicking (S403E) when immobilized GlyR $\beta$  loop S403A was tested versus GlyR $\beta$  loop S403E for binding of GFP-*syndapin I* using fluorescence-based Western blot analyses (Fig. 10A,B;  $p=0.0433$ ).

In contrast and as previously described (Specht et al., 2011), gephyrin binding showed a suppression of binding (Fig. 10C). Quantitative, fluorescence-based Western blot analyses showed that 15% less GFP-gephyrin E domain was bound to S403E mutated cytoplasmic GlyR $\beta$  loop compared with an S403A mutant representing the constitutive non-phosphorylated status (Fig. 10D; KO,  $p=0.0027$ ). Corresponding to this reduction in GlyR $\beta$  binding, more GFP-gephyrin E domain remained in the supernatant (Fig. 10C).

The promotion of *syndapin I* binding was more pronounced than the suppressive effect on gephyrin binding. *Syndapin I*

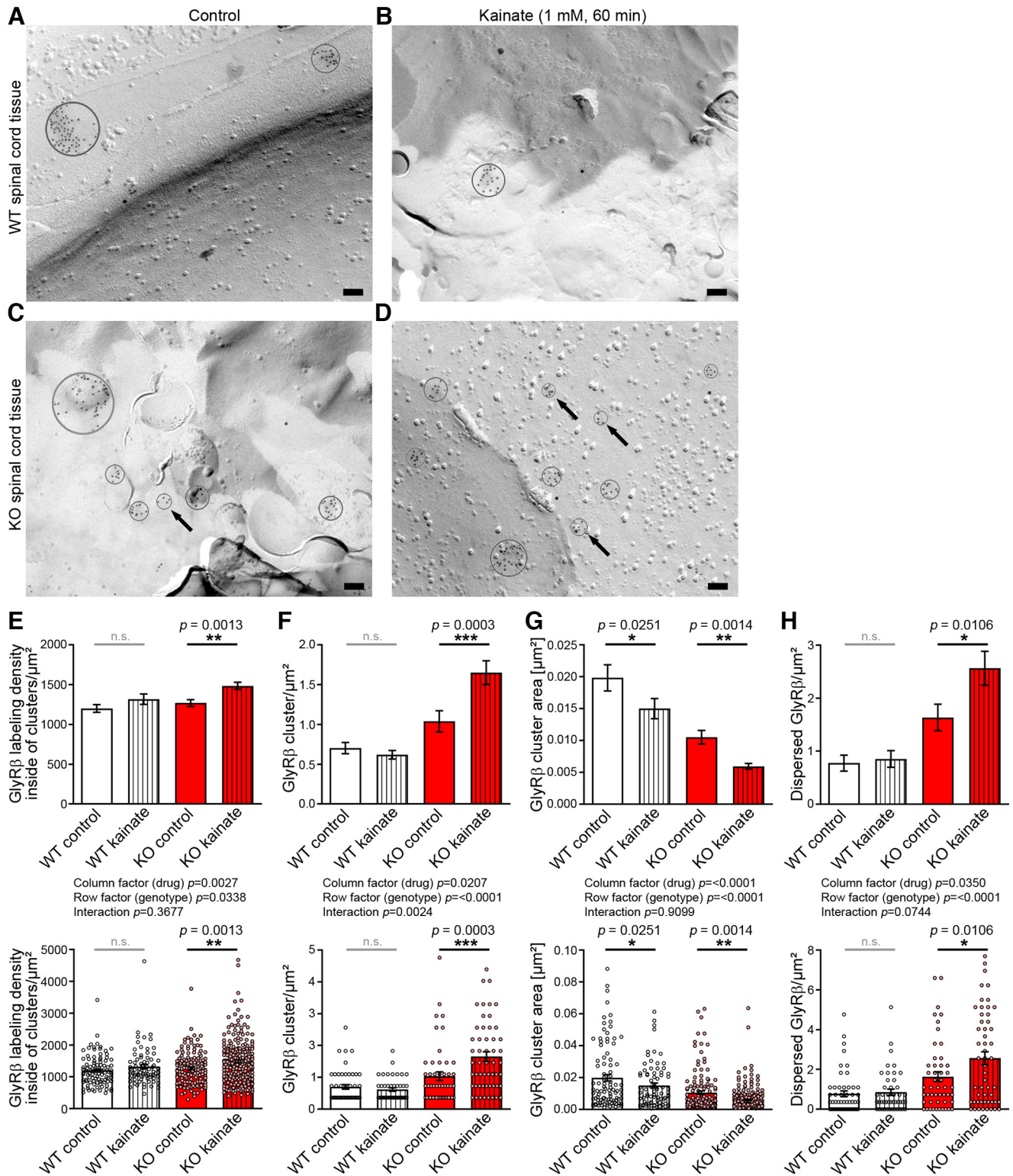


**Figure 9.** Kainate-treated spinal cords of *syndapin 1* KO mice show strong defects in GlyR $\beta$  field organization. **A–D**, TEM images of anti-GlyR $\beta$  immunogold-labeled, freeze-fractured spinal cord plasma membranes from WT (**A,B**) and *syndapin 1* KO mice (**C,D**), that either represented control (**A,C**) or were treated with 1 mM kainate for 60 min (**B,D**). Clusters are encircled. Average clusters are smaller when *syndapin 1* KO spinal cords were incubated with kainate particularly small clusters are pointed out with arrows in both *syndapin 1* KO control (**C**) and in kainate-treated *syndapin 1* KO spinal cord (**D**). Scale bars, 100 nm. **E–H**, Quantitative analyses of GlyR $\beta$  immunolabeling at the plasma membrane in WT and *syndapin 1* KO spinal cord samples addressing changes in receptor field organization and GlyR $\beta$  distribution caused by kainate treatment. Shown are determinations of the GlyR $\beta$  labeling density inside of clusters (**E**), GlyR $\beta$  cluster densities (**F**), GlyR $\beta$  cluster sizes (**G**), and the densities of dispersed anti-GlyR $\beta$  immunolabelings (**H**). For determinations of the overall GlyR $\beta$  immunolabeling densities, see Figure 8A. Data are mean  $\pm$  SEM, shown as bar plots and as bar/dot plots;  $n=96$  (WT control),  $n=76$  (WT kainate),  $n=139$  (KO control), and  $n=239$  (KO kainate) individual GlyR $\beta$  clusters, respectively, observed in  $n=50$  (WT control, see also data Fig. 2),  $n=49$  (KO control, see also data Fig. 2),  $n=45$  (WT kainate), and  $n=53$  (KO kainate) images from two independent spinal cord preparations from WT and *syndapin 1* KO mice. Two-way-ANOVA and Bonferroni post-test for control versus kainate comparisons (**E**, WT, not significant and KO,  $**p=0.0013$ , respectively; **F**, WT, not significant and KO,  $***p=0.0003$ , respectively; **G**, WT,  $*p=0.0251$ , and KO,  $**p=0.0014$ , respectively; **H**, WT, not significant and KO,  $*p=0.0106$ , respectively). For numerical data, see Extended Data Figure 9-1.

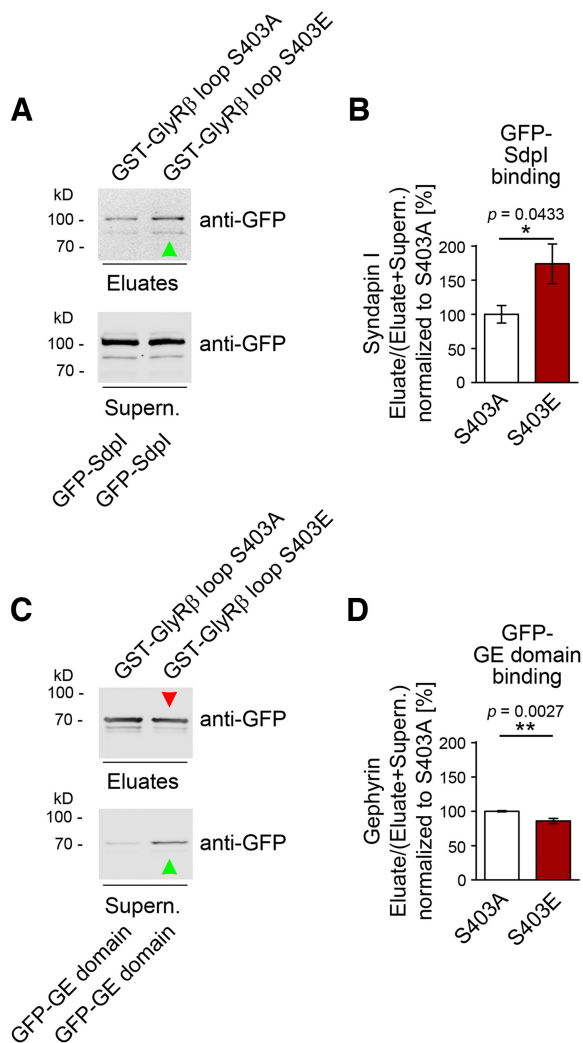


**Figure 10.** The PKC-dependent phosphorylation site S403 of GlyR $\beta$  is an important switch for diminishing gephyrin binding and simultaneously promoting the association of syndapin I. **A–D**, Quantitative Western blot analyses of coprecipitation experiments addressing the association of GFP-syndapin I (GFP-Sydn I) (**A,B**) and GFP-gephyrin E domain (GFP-GE domain) (**C,D**) expressed in HEK293 cells with mutants of the GlyR $\beta$  cytoplasmic loop mimicking a constitutively non-phosphorylated state (S403A) and a constitutively phosphorylated state (S403E), respectively, of the S403 PKC phosphorylation site of GlyR $\beta$ . Data are mean  $\pm$  SEM.  $n = 10$  (syndapin I binding);  $n = 8$  experiments (gephyrin binding). Arrowheads indicate bands with increased (green) and decreased (red) intensity, respectively. Mann–Whitney (**B**;  $*p = 0.0433$ ) and unpaired Student's  $t$  test (**D**;  $**p = 0.0027$ ), respectively. For numerical data, see Extended Data Figure 10-1.

I binding increased by  $\sim 75\%$  in relation to S403A. Both the reduction of gephyrin binding as well as the increase in syndapin I binding were statistically significant (Fig. 10B,D;  $p = 0.0433$  and  $p = 0.0027$ , respectively).

Our quantitative analyses thus demonstrated that gephyrin and syndapin I binding to GlyR $\beta$  are regulated by the PKC phosphorylation site S403 in an opposed manner. S403 phosphorylation may thus not only diminish gephyrin scaffolding to some extent but at the same time strongly promotes the coupling to syndapin I, which under the conditions of PKC activation by kainate then acts as crucial player in GlyR $\beta$  organization and endocytosis. Such a regulation would allow for efficient switching from gephyrin binding or simultaneous gephyrin/syndapin I binding of GlyR $\beta$ s under normal circumstances to syndapin I-mediated GlyR $\beta$  scaffolding and also to syndapin I-mediated GlyR $\beta$  endocytosis under conditions of kainate stimulation.

## Discussion

GlyRs are the major mediators of fast synaptic inhibition in the spinal cord and brainstem, but molecular mechanisms and cellular components that modulate synaptic plasticity in inhibitory synapses largely remained elusive. PKC activation, for example, via kainate receptor stimulation, was suggested to be involved, as such treatments led to increased lateral diffusion of GlyR from inhibitory synapses and to GlyR internalization (Specht et al., 2011; Sun et al., 2014). Our study identified syndapin I as critical player in kainate-induced GlyR $\beta$  internalization, in GlyR $\beta$  anchoring and in the organization of GlyR $\beta$  fields during both steady-state and kainate-induced synaptic rearrangements, as syndapin I was identified to be sensitive to GlyR $\beta$  phosphorylation at S403.

The syndapin I binding site in the cytoplasmic loop of GlyR $\beta$  is immediately adjacent to the binding site of gephyrin (Kim et al., 2006; del Pino et al., 2014). Some sequences that flank the gephyrin-binding site of GlyR $\beta$  were found to tune synaptic GlyR stabilization (Grünwald et al., 2018). This raised the question whether the two GlyR $\beta$  scaffolding proteins gephyrin and syndapin I act independently, influence each other, or even compete for GlyR $\beta$  binding. Our biochemical and quantitative ultrahigh-resolution imaging data showed that the relationship of gephyrin and syndapin I is complex. It includes some competition in GlyR $\beta$  binding but also cooperative action reflected by simultaneous GlyR $\beta$  binding. In line, although gephyrin is considered as the major GlyR $\beta$  scaffold protein (Kirsch et al., 1993; Feng et al., 1998), intriguingly also *syndapin I* KO led to strong defects in the organization of GlyR $\beta$  fields.

Ultrastructural views of GlyR $\beta$  fields obtained by combining freeze-fracturing, platinum-shadowing and immunogold labeling allowed for to our knowledge the first detailed, quantitative GlyR $\beta$  field evaluation at ultrastructural resolution. This advance is in line with a few reports demonstrating successful immunolabelings of integral membrane proteins in freeze-fractured membranes (Caruncho et al., 1993; Shigemoto et al., 1997; Kulik et al., 2006; Antal et al., 2008). Our ultrahigh-resolution analyses of spinal cord samples from WT and *syndapin I* KO mice demonstrated that *syndapin I* KO GlyR $\beta$  fields were only half the size of WT ones. Since in parallel the abundance of GlyR $\beta$  clusters and of dispersely localized GlyR $\beta$  rose sharply, *syndapin I* KO results in a fragmentation of GlyR $\beta$  fields.

Our EM results hereby were in line with reductions of the sizes and corresponding increases in puncta densities in our quantitative SIM analyses. Even the larger WT GlyR $\beta$  fields are below the resolution limit of conventional light microscopy (Specht et al., 2013; Maynard et al., 2021). This lack of resolution of at least classical immunofluorescence techniques explains why previous analyses failed to resolve the strong increase in GlyR $\beta$  clusters in *syndapin I* KO samples but instead reported an apparent disappearance of GlyR $\beta$  puncta in syndapin I-deficient neurons (del Pino et al., 2014). In line with the important role of syndapin I in the organization of GlyR $\beta$  fields unveiled by our (ultra)high-resolution studies, we also observed that the mobility of GlyR $\beta$  increased as a consequence of syndapin I deficiency. Syndapin I thus plays a critical role in GlyR $\beta$  anchoring and scaffolding.

This role of syndapin I is distinct of that of gephyrin, as gephyrin was unable to take over syndapin I's functions in the organization of GlyR $\beta$  fields. Importantly, a putative impairment of gephyrin expression was not observed in *syndapin I* KO spinal cords, but *syndapin I* KO led to a decoupling of a certain proportion of GlyR $\beta$ s from the scaffolds in inhibitory synapses. This decoupling was observable in our studies in form of both small assemblies of GlyR $\beta$  immunogold labels and dispersed anti-GlyR $\beta$  immunogold labels. In contrast, neither the gephyrin scaffolds by themselves nor



the dense packaging of GlyR $\beta$ s inside of the GlyR $\beta$  fields seemed affected by *syndapin I* KO. GlyR $\beta$  packaging inside of GlyR $\beta$  fields thus seems to be specifically brought about by gephyrin. Also very recent examinations of heterozygous oscillator mice, a neuromotor disease model, with more classical super-resolution and transmission EM of sections did not show any obvious GlyR packaging defects (Maynard et al., 2021).

Gephyrin is known to form a rigid, highly ordered two-dimensional protein scaffold to which GlyR $\beta$ s can dock in high density (Sola et al., 2004; Bedet et al., 2006). Syndapin I, in contrast, dimerizes (Kessels and Qualmann, 2006) reconstituting a functional F-BAR domain interacting with defined membrane lipids and topologies (Itoh et al., 2005; Dharmalingam et al., 2009; Wang et al., 2009; Schneider et al., 2014). This could provide GlyR $\beta$ s with extended contacts to (curved) membrane surfaces.

Furthermore, syndapin I's SH3 domain interacts with different membrane trafficking and actin cytoskeletal components (Qualmann et al., 1999; Kessels and Qualmann, 2002; Ahuja et al., 2007; Schwintzer et al., 2011; Izadi et al., 2021). It is therefore plausible that the molecular properties of syndapin I's F-BAR and SH3 domain contribute to GlyR anchoring and, in contrast to gephyrin's role in receptor packaging, may bring about rather peripheral interactions of GlyR $\beta$  fields and/or hold together receptor subfields and thereby be critical for the overall GlyR $\beta$  field architecture. Furthermore, it is conceivable that these molecular properties may also underlie the identified role of syndapin I in kainate-induced GlyR $\beta$  internalization.

With syndapin I, we unveil the first endocytic protein crucial for the internalization of endogenous GlyRs identified by KO analyses. In both cultured spinal cord neurons and in spinal cord tissue, kainate-induced endocytosis of endogenous GlyRs was completely abolished by *syndapin I* KO.

Interestingly, kainate receptor activation-induced GlyR endocytosis was observed to be calcium- and PKC-dependent using pan-GlyR antibodies (Sun et al., 2014). A PKC involvement in internalization of GlyR $\alpha$ 1s exogenously expressed in HEK293 cells had been shown (Huang et al., 2007; Breitingner et al., 2018). But whether the synaptic GlyR $\beta$  subunits are internalized and whether such internalizations indeed also occur in neurons remained unaddressed. Our quantitative ultrastructural analyses, which specifically addressed plasma membrane-localized clusters of the synaptic and gephyrin-bound, as well as syndapin I-bound GlyR $\beta$  subunit, showed a decrease of GlyR $\beta$  immunolabeling at the plasma membrane when dissociated cultures of WT spinal cord neurons were stimulated with kainate. Thus, the reduced synaptic transmission capability of GlyR caused by kainate treatment (Specht et al., 2011; Sun et al., 2014) clearly correlated with a reduced availability of specifically GlyR $\beta$  at the plasma membrane. Our quantitative EM examinations showed that, in both dissociated cultures of primary spinal cord neurons but importantly also in spinal cord tissue of WT mice, more than one-fourth of all GlyR $\beta$  at the plasma membrane of WT spinal cords were internalized upon stimulation with kainate. These data were exactly in line with our Apotome-based determinations of GlyR levels with and without kainate stimulation at the surface of cultured neurons using pan-GlyR antibodies. Our work in spinal cord tissue clearly proved that GlyR internalization also occurred in intact spinal cords. Thus, this neuron-intrinsic property of this plastic rearrangement of GlyRs is not merely a cell culture phenomenon but is also of physiological relevance in spinal cords.

Intriguingly, the effects of kainate treatments on the GlyR $\beta$  receptor fields that remained present at the plasma membrane were moderate as long as syndapin I was present. The GlyR $\beta$

clusters were  $\sim$ 25% smaller when kainate-treated WT spinal cords were compared with control. As neither their density nor the density of dispersed GlyR $\beta$ s increased significantly differed and also the GlyR $\beta$  packaging inside of clusters remained unchanged, the drop of overall GlyR $\beta$  levels at the plasma membrane detected in kainate-stimulated samples seemed to be brought about by GlyR decoupling from the still prevailing GlyR fields. In form of small receptor assemblies and single receptors, these receptors were apparently then internalized. Therefore, in WT spinal cords, these scaffold-decoupled receptors were not detected at the plasma membrane anymore.

Importantly, our biochemical examinations showed that this decoupling from gephyrin scaffolds was not only GlyR $\beta$  S403 phosphorylation-driven but that mimicking GlyR $\beta$  S403 phosphorylation also increased the syndapin I binding. The identified regulatory mechanism thus seems to tip the balance from gephyrin-mediated GlyR scaffolding and cooperative functions of syndapin I in GlyR field organization and GlyR scaffolding (i.e., both proteins holding GlyR $\beta$ ) toward GlyR dissociation from the gephyrin scaffold and promotion of syndapin I binding. Once liberated from gephyrin's scaffolding functions, syndapin I apparently does not just hold GlyR $\beta$  clusters but promotes their internalization. In line, the defects in GlyR $\beta$  field organization observed under kainate stimulation in *syndapin I* KO spinal cords were strong and, for example, included an even further fragmentation of GlyR $\beta$  fields than already observed by *syndapin I* KO alone.

Syndapin I thus acts as a scaffold protein regulating the size and density of GlyR $\beta$  clusters and controlling GlyR $\beta$  mobility in the neuronal plasma membrane. Additionally, syndapin I promotes GlyR $\beta$  internalization once GlyR $\beta$ s become decoupled from gephyrin scaffolds. Syndapin I thereby represents an important GlyR $\beta$  interaction partner controlling the number and organization of GlyR fields at inhibitory postsynapses in multiple ways both during steady state and during kainate-induced synaptic rearrangement. Molecular mechanisms modulating GlyR numbers at glycinergic synapses fine-tune synaptic efficacy and are thus important to maintain proper neuronal excitability and to regulate excitation-inhibition balance in the CNS.

## References

- Ahuja R, Pinyol R, Reichenbach N, Custer L, Klingensmith J, Kessels MM, Qualmann B (2007) Cordon-bleu is an actin nucleation factor and controls neuronal morphology. *Cell* 131:337–350.
- Alvarez FJ (2017) Gephyrin and the regulation of synaptic strength and dynamics at glycinergic inhibitory synapses. *Brain Res Bull* 129:50–65.
- Antal M, Fukazawa Y, Eordogh M, Muszil D, Molnar E, Itakura M, Takahashi M, Shigemoto R (2008) Numbers, densities, and colocalization of AMPA- and NMDA-type glutamate receptors at individual synapses in the superficial spinal dorsal horn of rats. *J Neurosci* 28:9692–9701.
- Bedet C, Bruusgaard JC, Vergo S, Groth-Pedersen L, Eimer S, Triller A, Vannier C (2006) Regulation of gephyrin assembly and glycine receptor synaptic stability. *J Biol Chem* 281:30046–30056.
- Braun A, Pinyol R, Dahlhaus R, Koch D, Fonarev P, Grant BD, Kessels MM, Qualmann B (2005) EHD proteins associate with syndapin I and II and such interactions play a crucial role in endosomal recycling. *Mol Biol Cell* 16:3642–3658.
- Breitingner U, Bahnassawy LM, Janzen D, Roemer V, Becker CM, Villmann C, Breitingner HG (2018) PKA and PKC modulators affect ion channel function and internalization of recombinant  $\alpha$ 1 and  $\alpha$ 1- $\beta$  glycine receptors. *Front Mol Neurosci* 11:154.
- Caruncho HJ, Puia G, Slobodyansky E, da Silva PP, Costa E (1993) Freeze-fracture immunocytochemical study of the expression of native and recombinant GABA<sub>A</sub> receptors. *Brain Res* 603:234–242.
- Choquet D, Hosy E (2020) AMPA receptor nanoscale dynamic organization and synaptic plasticities. *Curr Opin Neurobiol* 63:137–145.

- del Pino I, Koch D, Schemm R, Qualmann B, Betz H, Paarmann I (2014) Proteomic analysis of glycine receptor beta subunit (GlyRbeta)-interacting proteins: evidence for syndapin I regulating synaptic glycine receptors. *J Biol Chem* 289:11396–11409.
- Dharmalingam E, Haeckel A, Pinyol R, Schwintzer L, Koch D, Kessels MM, Qualmann B (2009) F-BAR proteins of the syndapin family shape the plasma membrane and are crucial for neuromorphogenesis. *J Neurosci* 29:13315–13327.
- Diering GH, Huganir RL (2018) The AMPA receptor code of synaptic plasticity. *Neuron* 100:314–329.
- Dumoulin A, Triller A, Kneussel M (2010) Cellular transport and membrane dynamics of the glycine receptor. *Front Mol Neurosci* 2:28.
- Dutertre S, Becker CM, Betz H (2012) Inhibitory glycine receptors: an update. *J Biol Chem* 287:40216–40223.
- Feng G, Tintrup H, Kirsch J, Nichol MC, Kuhse J, Betz H, Sanes JR (1998) Dual requirement for gephyrin in glycine receptor clustering and molybdoenzyme activity. *Science* 282:1321–1324.
- Grosskreutz J, Haastert K, Dewil M, Van Damme P, Callewaert G, Robberecht W, Dengler W, Van Den Bosch L (2007) Role of mitochondria in kainate-induced fast  $Ca^{2+}$  transients in cultured spinal motor neurons. *Cell Calcium* 42:59–69.
- Grudzinska J, Schemm R, Haeger S, Nicke A, Schmalzing G, Betz H, Laube B (2005) The beta subunit determines the ligand binding properties of synaptic glycine receptors. *Neuron* 45:727–739.
- Grünewald N, Jan A, Salvatico C, Kress V, Renner M, Triller A, Specht CG, Schwarz G (2018) Sequences flanking the gephyrin-binding site of GlyRbeta tune receptor stabilization at synapses. *eNeuro* 5:ENEURO.0042-17.2018.
- Gustafsson MG (2005) Nonlinear structured-illumination microscopy: wide-field fluorescence imaging with theoretically unlimited resolution. *Proc Natl Acad Sci USA* 102:13081–13086.
- Haag N, Schüler S, Nietzsche S, Hübner CA, Strenzke N, Qualmann B, Kessels MM (2018) The actin nucleator Cobl is critical for centriolar positioning, postnatal planar cell polarity refinement, and function of the cochlea. *Cell Rep* 24:2418–2431.
- Huang R, He S, Chen Z, Dillon GH, Leidenheimer NJ (2007) Mechanisms of homomeric alpha1 glycine receptor endocytosis. *Biochemistry* 46:11484–11493.
- Itoh T, Erdmann KS, Roux A, Habermann B, Werner H, De Camilli P (2005) Dynamin and the actin cytoskeleton cooperatively regulate plasma membrane invagination by BAR and F-BAR proteins. *Dev Cell* 9:791–804.
- Izadi M, Schlobinski D, Lahr M, Schwintzer L, Qualmann B, Kessels MM (2018) Cobl-like promotes actin filament formation and dendritic branching using only a single WH2 domain. *J Cell Biol* 217:211–230.
- Izadi M, Seemann E, Schlobinski D, Schwintzer L, Qualmann B, Kessels MM (2021) Functional interdependence of the actin nucleator Cobl and Cobl-like in dendritic arbor development. *Elife* 10:e67718.
- Kasaragod VB, Schindelin H (2018) Structure-function relationships of glycine and GABAA receptors and their interplay with the scaffolding protein gephyrin. *Front Mol Neurosci* 11:317.
- Kessels MM, Qualmann B (2002) Syndapins integrate N-WASP in receptor-mediated endocytosis. *EMBO J* 21:6083–6094.
- Kessels MM, Qualmann B (2006) Syndapin oligomers interconnect the machineries for endocytic vesicle formation and actin polymerization. *J Biol Chem* 281:13285–13299.
- Kessels MM, Qualmann B (2015) Different functional modes of BAR domain proteins in formation and plasticity of mammalian postsynapses. *J Cell Sci* 128:3177–3185.
- Kim EY, Schrader N, Smolinsky B, Bedet C, Vannier C, Schwarz G, Schindelin H (2006) Deciphering the structural framework of glycine receptor anchoring by gephyrin. *EMBO J* 25:1385–1395.
- Kirsch J, Betz H (1995) The postsynaptic localization of the glycine receptor-associated protein gephyrin is regulated by the cytoskeleton. *J Neurosci* 15:4148–4156.
- Kirsch J, Wolters I, Triller A, Betz H (1993) Gephyrin antisense oligonucleotides prevent glycine receptor clustering in spinal neurons. *Nature* 366:745–748.
- Koch D, et al. (2011) Proper synaptic vesicle formation and neuronal network activity critically rely on syndapin I. *EMBO J* 30:4955–4969.
- Koch D, Westermann M, Kessels MM, Qualmann B (2012) Ultrastructural freeze-fracture immunolabeling identifies plasma membrane-localized syndapin II as a crucial factor in shaping caveolae. *Histochem Cell Biol* 138:215–230.
- Koch N, Koch D, Krueger S, Tröger J, Sabanov V, Ahmed T, McMillan LE, Wolf D, Montag D, Kessels MM, Balschun D, Qualmann B (2020) Syndapin I loss-of-function in mice leads to schizophrenia-like symptoms. *Cereb Cortex* 30:4306–4324.
- Kuzhandaivel A, Nistri A, Mladinic M (2010) Kainate-mediated excitotoxicity induces neuronal death in the rat spinal cord in vitro via a PARP-1 dependent cell death pathway (Parthanatos). *Cell Mol Neurobiol* 30:1001–1012.
- Kulik A, et al. (2006) Compartment-dependent colocalization of Kir3.2-containing  $K^{+}$  channels and GABAB receptors in hippocampal pyramidal cells. *J Neurosci* 26:4289–4297.
- Langhofer G, Schaefer N, Maric HM, Keramidis A, Zhang Y, Baumann P, Blum R, Breiting U, Stromgaard K, Schlosser A, Kessels MM, Koch D, Qualmann B, Breiting HG, Lynch JW, Villmann C (2020) A novel glycine receptor variant with startle disease affects syndapin I and glycinergic inhibition. *J Neurosci* 40:4954–4969.
- Legendre P, Muller E, Badiu CI, Meier J, Vannier C, Triller A (2002) Desensitization of homomeric alpha1 glycine receptor increases with receptor density. *Mol Pharmacol* 62:817–827.
- Lévi S, Schweizer C, Bannai H, Pascual O, Charrier C, Triller A (2008) Homeostatic regulation of synaptic GlyR numbers driven by lateral diffusion. *Neuron* 59:261–273.
- Maynard SA, Rostaing P, Schaefer N, Gemin O, Candat A, Dumoulin A, Villmann C, Triller A, Specht CG (2021) Identification of a stereotypic molecular arrangement of endogenous glycine receptors at spinal cord synapses. *eLife* 10:e74441.
- Qualmann B, Roos J, DiGregorio PJ, Kelly RB (1999) Syndapin I, a synaptic dynamin-binding protein that associates with the neural Wiskott-Aldrich syndrome protein. *Mol Biol Cell* 10:501–513.
- Qualmann B, Koch D, Kessels MM (2011) Let's go bananas: revisiting the endocytic BAR code. *EMBO J* 30:3501–3515.
- Schneider K, Seemann E, Liebmann L, Ahuja R, Koch D, Westermann M, Hübner CA, Kessels MM, Qualmann B (2014) ProSAP1 and membrane nanodomain-associated syndapin I promote postsynapse formation and function. *J Cell Biol* 205:197–215.
- Schwintzer L, Koch N, Ahuja R, Grimm J, Kessels MM, Qualmann B (2011) The functions of the actin nucleator Cobl in cellular morphogenesis critically depend on syndapin I. *EMBO J* 30:3147–3159.
- Seemann E, Sun M, Krueger S, Tröger J, Hou W, Haag N, Schüler S, Westermann M, Huebner CA, Romeike B, Kessels MM, Qualmann B (2017) Deciphering caveolar functions by syndapin III KO-mediated impairment of caveolar invagination. *eLife* 6:e29854.
- Shigemoto R, Kinoshita A, Wada E, Nomura S, Ohishi H, Takada M, Flor PJ, Neki A, Abe T, Nakanishi S, Mizuno N (1997) Differential presynaptic localization of metabotropic glutamate receptor subtypes in the rat hippocampus. *J Neurosci* 17:7503–7522.
- Sola M, Bavro VN, Timmins J, Franz T, Ricard-Blum S, Schoehn G, Ruigrok RW, Paarmann I, Saiyed T, O'Sullivan GA, Schmitt B, Betz H, Weissenhorn W (2004) Structural basis of dynamic glycine receptor clustering by gephyrin. *EMBO J* 23:2510–2519.
- Specht CG, Grünewald N, Pascual O, Rostgaard N, Schwarz G, Triller A (2011) Regulation of glycine receptor diffusion properties and gephyrin interactions by protein kinase C. *EMBO J* 30:3842–3853.
- Specht CG, Izeddin I, Rodriguez PC, El Beheiry M, Rostaing P, Darzacq X, Dahan M, Triller A (2013) Quantitative nanoscopy of inhibitory synapses: counting gephyrin molecules and receptor binding sites. *Neuron* 79:308–321.
- Sun H, Lu L, Zuo Y, Wang Y, Jiao Y, Zeng WZ, Huang C, Zhu MX, Zamponi GW, Zhou T, Xu TL, Cheng J, Li Y (2014) Kainate receptor activation induces glycine receptor endocytosis through PKC deSUMOylation. *Nat Commun* 5:4980.
- Taccola G, Margaryan G, Mladinic M, Nistri A (2008) Kainate and metabolic perturbation mimicking spinal injury differentially contribute to early damage of locomotor networks in the in vitro neonatal rat spinal cord. *Neuroscience* 155:538–555.
- Tröger J, Hoischen C, Perner B, Monajembashi S, Barbotin A, Löscherberger A, Eggeling C, Kessels MM, Qualmann B, Hemmerich P (2020) Comparison of multiscale imaging methods for brain research. *Cells* 9:1377.
- Wang Q, Navarro MV, Peng G, Molinelli E, Goh SL, Judson BL, Rajashankar KR, Sondermann H (2009) Molecular mechanism of membrane constriction and tubulation mediated by the F-BAR protein Paccin/Syndapin. *Proc Natl Acad Sci USA* 106:12700–12705.
- Wolf D, Hofbrucker MacKenzie SA, Izadi M, Seemann E, Steiniger F, Schwintzer L, Koch D, Kessels MM, Qualmann B (2019) Ankyrin repeat-containing N-Ank proteins shape cellular membranes. *Nat Cell Biol* 21:1191–1205.